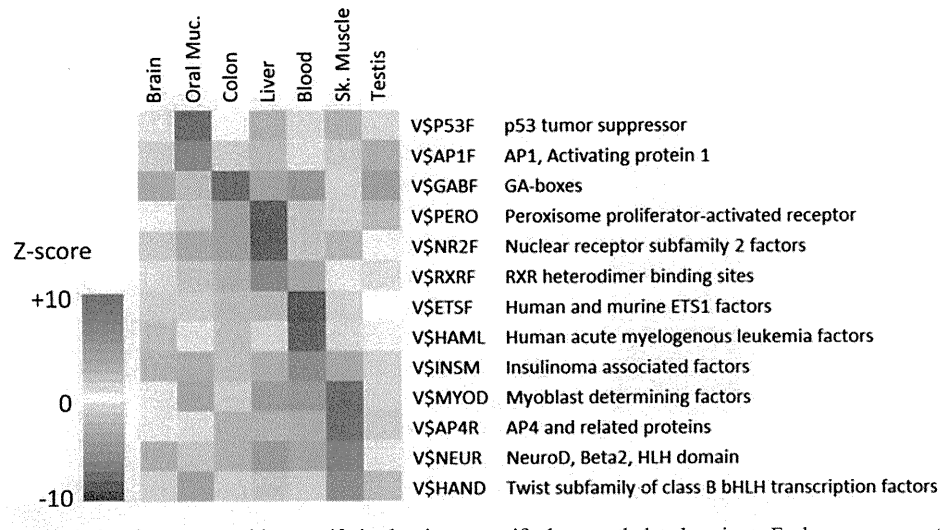

Figure 4. Enrichment of transcription factor recognition motifs in the tissue-specific hypomethylated regions. Each row represents a cis-regulatory module family with significant over-representation relative to a random set of mammalian promoters (Z-score > 8.0). Each column represents a tissue type. Four tissues (oral mucosa, liver, blood and skeletal muscle) show some specific enrichment of their master regulators binding motifs, respectively.

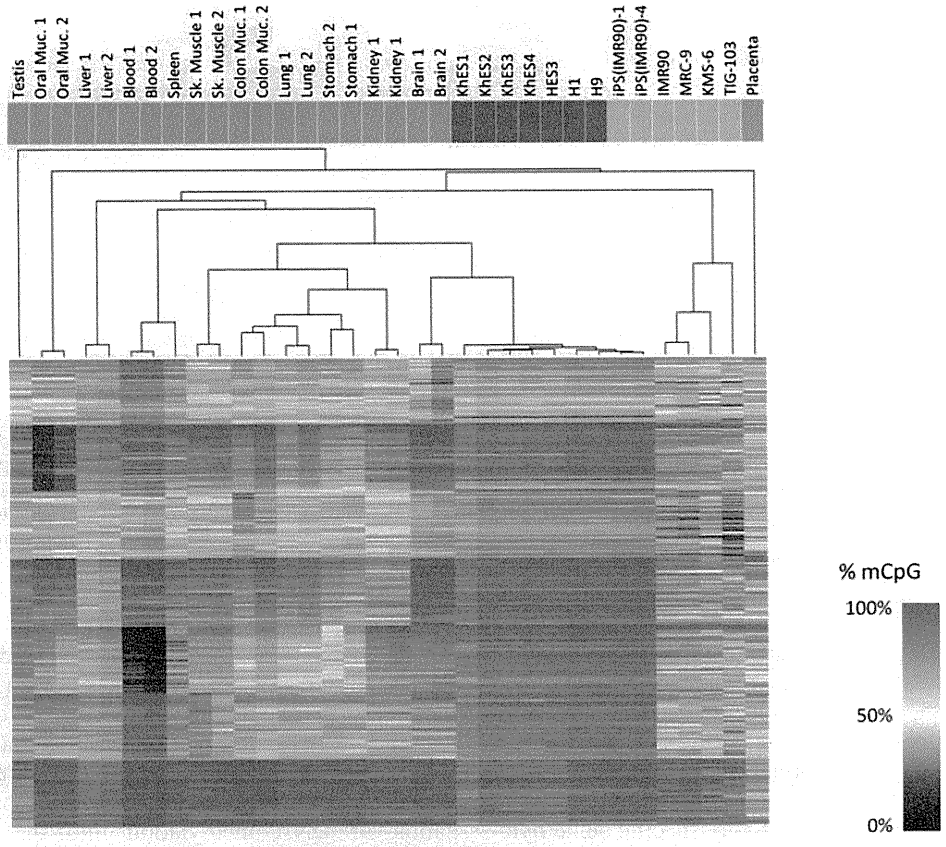

Figure 5. Hierarchical clustering analysis of human somatic tissues and normal cells. The dendrogram in the upper panel was obtained on the basis of the representative gene sets of tissue-specific hypomethylation using average linkage correlation. Each row represents a CpG locus (250 tissue-specific hypomethylation for each) and each column represents a sample. The colored boxes above the dendrogram indicate the nature of the samples; human somatic tissues (blue), human ES cells (red), human iPS cells (orange) and human primary fibroblast (green). The color scale bar at the right side shows the percentage of the methylation level (0–100%).

Active demethylation is observed in the paternal genome of an embryo during the first few days (33,34). In this process, demethylation occurs globally except for the limited foci such as imprinting control regions and centromeric and pericentromeric heterochromatin (35). Although recent reports suggested the ten-eleven translocation (TET) family proteins,

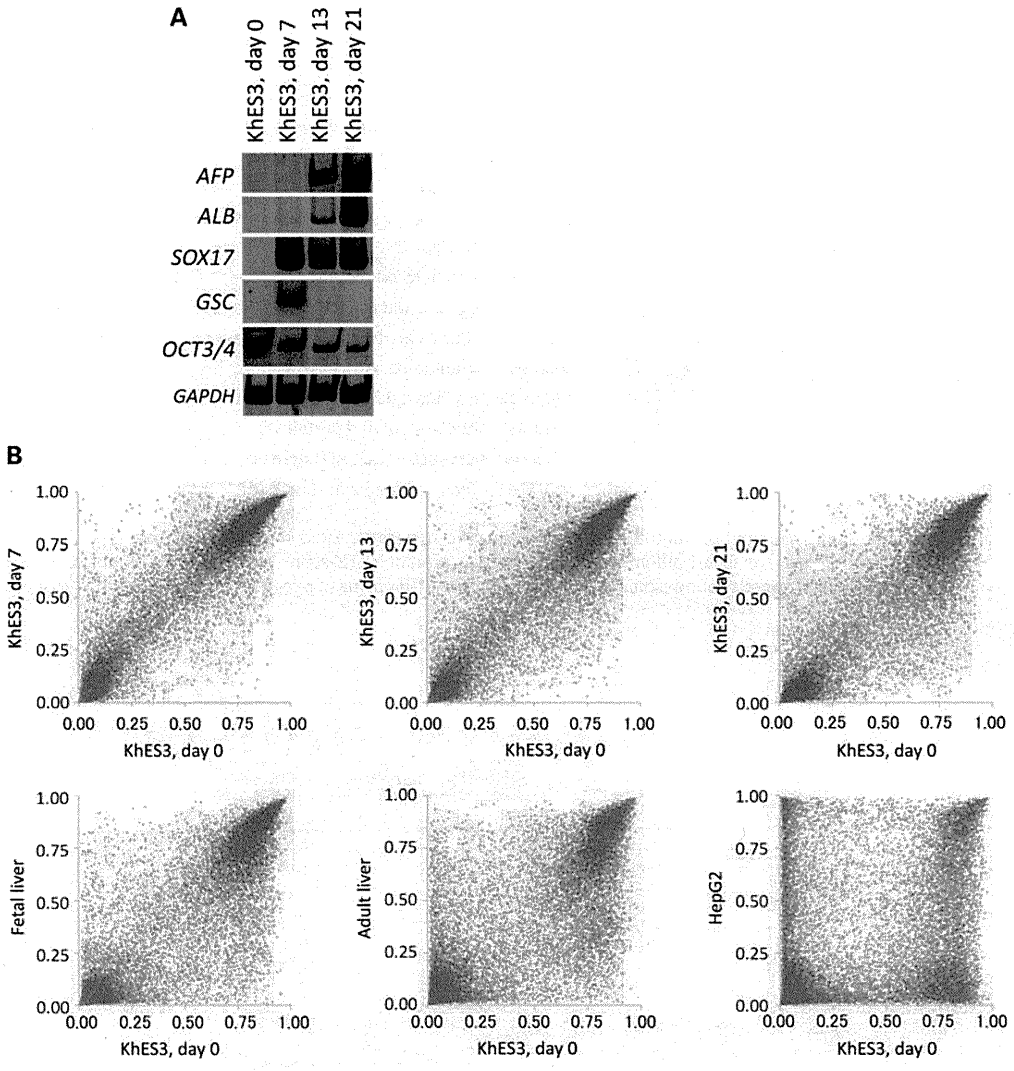

Figure 6. *In vitro* demethylation of liver-specific hypomethylated genes during hepatic differentiation (**A**) RT–PCR analysis of endodermal and hepatic differentiation markers in ES cells and differentiated cells (**B**) Global comparison among undifferentiated ES cells and differentiated cells, human fetal liver, adult liver and HepG2 cells. Liver-specific hypomethylated genes are indicated as red dots, overlapping with the others (blue). (**C**) Examples of gradually demethylated genes during *in vitro* differentiation into hepatic lineages. The bar graphs show the methylation levels of the genes that show gradual demethylation (~20% decrease) in day 21 of *in vitro* differentiation. (**D**) The liver-specific hypomethylated region around the *APOA1* gene. In the upper panel of the UCSC browser, nine black boxes indicate the position of PCR amplicons in a MassARRAY analysis. The methylation levels around the *APOA1* gene among ES cells and adult liver tissues are shown in the lower panel.

TET1, TET2 and TET3, are candidate proteins responsible for the erasure process through an oxidative demethylation pathway (32,36), further investigations are needed. The unexpected dynamics of DNA methylation during cellular differentiation might give us an important clue to elucidate the mechanism of cell fate determination during embryogenesis.

An alternative explanation for the tissue-specific demethylation seen in CpG-poor promoters is passive demethylation, which is usually observed in asymmetric cell division or highly proliferating cells like cancer cells. Inhibiting maintenance of cytosine methylation of the template strand could result in dilution of methylation in differentiated daughter cells. According to this scenario, transcription factor-related inhibition of DNA methyltransferase at the timing of cell division might be necessary because the developmental hypomethylation we observed here occurs not in a genome-wide manner but in a regional manner. Indeed, the enrichment of transcription factor-binding motifs is seen at the demethylated regions in a tissue-specific manner. Recently, it was shown that mitotically retained transcription factors are associated with the asymmetric cell division in some contexts (37,38). If sustained binding of transcription factors inhibits propagation of DNA methylation into the newly synthesized strand, transcription factor-driven demethylation will be inherited in proliferating cells. In our study, we examined *in vitro* differentiation in a series of promoters and found that a wave of demethylation develops from the TSS of *APOA1* and *ITIH3* promoters. Once the binding of transcription factors at demethylated regions induces gene expression in the tissue progenitor cells, sustained induction in response to appropriate extrinsic stimuli may result in loss of propagation of DNA methylation marks in the promoter regions for

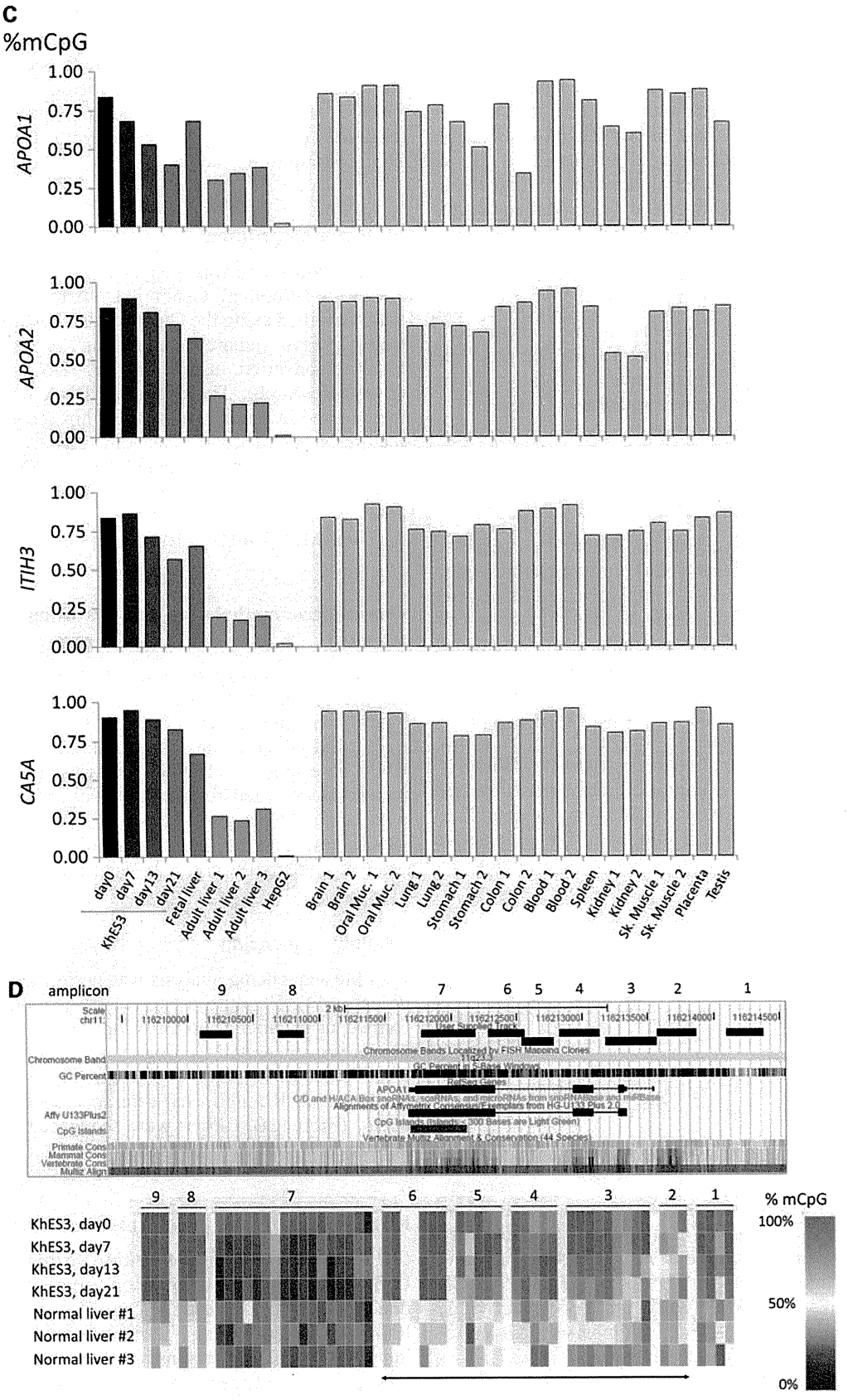

Figure 6. (Continued).

long-lasting maintenance of a transcriptionally active state. Subsequently, in this model, chromatin conformation changes in terminally differentiated cells would expand the demethylated regions and contribute to the establishment of stable and highly efficient expression of specific gene subsets.

Growing evidence suggests that forced induction of master regulator genes has the potential to change the fate of lineage-restricted cells, even in terminally differentiated cells (39–41). We identified restoration of methylation during reprogramming into iPS cells. The feasibility of cell reprogramming suggests that differentiated cells still have much more plasticity in the epigenetic status including DNA methylation than we had expected. Further analysis of methylation changes might provide novel insight into mechanisms that will generate a transcriptional repertoire for variable cell lineages and give us useful clues to control cell fate fixation, which might be applicable for regenerative medicine.

MATERIALS AND METHODS

Genomic DNA from human normal tissues

Frozen tissues of the brain, lung, liver and kidney were obtained from surgical specimens. Patients undergoing surgical resection at the Tokyo University General Hospital provided tissue after obtaining informed consent. Buccal swabs of oral mucosa, peripheral blood and placental tissue were from healthy volunteers. This study was certified by the Ethics Committee of Tokyo University. Genomic DNA from these clinical samples was extracted using the QIAamp DNA Mini Kit (QIAGEN). Genomic DNA of further individuals was purchased from BioChain (details are listed in Supplementary Material, Table S1). For the methylation-negative control, totally unmethylated genomic DNA was synthesized by a whole-genome amplification system, GenomiPhi (GE healthcare). For a positive control, fully methylated genomic DNA was generated by *Sss*.I CpG methylase (New England Biolabs) treatment of lymphocyte DNA.

Human ES cell lines

Human ES cell lines, KhES1, KhES2, KhES3, KhES4, were established and maintained as described previously (42). Human ES cell lines (H1, H9) and human iPS cell lines [iPS(IMR90)-1 and iPS(IMR90)-4] were obtained from WiCell Research Institute. HES3 cell line was obtained from ES Cell International.

Briefly, undifferentiated human ES cells were maintained on a feeder layer of MEF in DMEM/F12 (Sigma) supplemented with 20% KSR, l-Glu, NEAA and β-ME under 3% CO_2. To passage ES cells, ES cell colonies were detached from the feeder layer by treatment with 0.25% trypsin and 0.1 mg/ml of collagenase IV in PBS containing 20% KSR and 1 mm of $CaCl_2$ at 37°C for 5 min, followed by the addition of culture medium. ES cell clumps were disaggregated into smaller pieces by gentle pipetting.

An *in vitro* differentiation experiment was performed following the reported method, with some modification (43). Briefly, KhES3 cells were cultured in differentiation medium [RPMI supplemented with human recombinant activin A (100 ng/ml) and defined FBS]. FBS concentrations were 0% for the first 24 h, 0.2% for the second 48 h and 2.0% for subsequent days of differentiation. Media were replaced every 2 days with fresh differentiation medium supplemented with growth factors. ES cells were cultured in differentiation medium (DMEM supplemented with 10% KSR, Dex and HGF) for up to 30 days.

Methylation profiling

Methylation status was analyzed using HumanMethylation27 BeadChip (Illumina). Genomic DNA for methylation profiling was quantified using the Quant-iT dsDNA BR Assay Kit (Invitrogen). Five hundred nanograms of genomic DNA was bisulfite-converted using an EZ DNA Methylation Kit (Zymo Research). The converted DNA was amplified, fragmented and hybridized to a BeadChip according to the manufacturer's instructions. The raw signal intensity for both methylated (M) and unmethylated (U) DNA was measured using a BeadArray Scanner (Illumina). The methylation level of the each individual CpG is obtained using the formula (M)/(M)+(U)+100 by the GenomeStudio (Illumina).

Quantitative methylation analysis using the MassARRAY system

Bisulfite treatment of genomic DNA was performed using an EZ Methylation Kit (Zymo Research). Primer sequences are given in Supplementary Material, Table S4. This system utilizes MALDI-TOF mass spectrometry in combination with RNA base-specific cleavage (MassCLEAVE). A detectable pattern is analyzed for the methylation status. Mass spectra were acquired using a MassARRAY Compact MADLI-TOF (Sequenom) and spectra's methylation ratios were generated using Epityper software v1.0 (Sequenom).

Bisulfite sequencing

Bisulfite sequencing analysis was performed as described previously (44). Bisulfite treatment of genomic DNA was performed using an EZ Methylation Kit (Zymo Research). All primer sequences and melting temperatures for the polymerase chain reaction (PCR) are given in Supplementary Material, Table S4. PCR amplicons were subcloned into the pGEM-T vector (Promega). Clones were sequenced using PRISM3100 Sequencer (Applied Biosystems).

RNA extraction and gene expression microarray analysis

Genome-wide analysis of mRNA expression levels using U133plus2.0 human expression array® (Affymetrix) was done essentially as described previously (45). Briefly, total RNA was isolated using TRIzol reagent (Invitrogen), according to the manufacturer's instructions. One microgram of RNA was used for the generation of double-stranded cDNA with the SuperScript Double-Stranded cDNA Synthesis Kit (Invitrogen) according to the manufacturer's protocol. Double-stranded cDNAs were hybridized to the microarray.

Reverse transcription–polymerase chain reaction analysis

RNA extraction and reverse transcription–polymerase chain reaction (RT–PCR) were done as described (46). Total RNA was extracted using TRI Reagent (Sigma-Aldrich) or the RNeasy micro-kit (Qiagen) and then treated with DNase (Sigma-Aldrich). Three micrograms of RNA was reverse-transcribed using Moloney Murine Leukemia Virus reverse transcriptase (Toyobo, Japan) and oligo(dT) primers (Toyobo). The primer sequences are shown in Supplementary Material, Table S4. The PCR conditions for each cycle were as follows: denaturation at 96°C for 30 s, annealing at 60°C for 2 s and extension at 72°C for 45 s. RT–PCR products were separated by 5% non-denaturing polyacrylamide gel electrophoresis, stained with SYBR Green I (Molecular Probes), and visualized using a Gel Logic 200 Imaging System (Kodak).

Definition of probe classes and promoter classes

We classified 27 578 probes into three categories: HCG, ICG and LCG. Each probe position was defined with respect to the position of a given CpG site. We determined the GC content and the ratio of observed versus expected CpG dinucleotides in a surrounding 500 bp window. The CpG ratio was calculated using the following formula: (number of CpGs × number of bp) (number of Cs × number of Gs). Three categories of probes were determined as follows: (i) HCGs (8098 probes) covering a 500 bp area with a CpG ratio above 0.75 and GC content above 55%; (ii) LCGs (8374 probes) excluded from a 500 bp area with a CpG ratio above 0.48; and (iii) ICGs (11 106 probes) that could not be categorized as either HCGs or LCGs.

Clustering analysis

To analyze the similarity of the methylation levels among human somatic tissues, ES cells and iPS cells, we used the data set of tissue-specific hypomethylation selected in Figure 2A for the cluster analysis. We applied a hierarchical clustering algorithm using the uncentered correlation coefficient as the measure of similarity and average linkage clustering (47) and visualized the dendrogram and the heatmap using TreeView (48).

GO functional annotation analysis

GO functional annotations for differentially hypomethylated and hypermethylated gene sets were performed using the Database for Annotation, Visualization and Integrated Discovery (DAVID) Bioinformatic Resources v6.7 (http://niaid.abcc.ncifcrf.gov/ home.jsp). The lists of 250 gene symbols that show specific hypermethylation or hypermethylation for each tissue were submitted and DAVID default population background (*Homo sapiens*) was chosen to detect significantly over-represented GO biological processes (GOTERM BP-FAT). *P*-values were calculated by a modified Fisher's exact test and adjusted for multiple hypotheses testing using Bonferroni correction. The three GO terms with the most significant *P*-value and the number of genes involved in the term were listed for each tissue.

Enrichment analysis of transcription factor-binding motifs

To determine over-represented transcription factor-binding sites in tissue-specific hypomethylated and hypermethylated regions, sequences around the probe within a 500 bp window were screened for the presence of binding sites using Genomatix RegionMiner (http://www.genomatix.de, matrix library version 7.1). The number of binding site motifs was determined and over-representation over the background of random mammalian promoter sequences was calculated as the *Z*-score. Transcription factor families with a Z-score greater than 8.0 were considered highly significant. The *Z*-scores of these representative TF modules are visualized in the heatmap using TreeView (48).

SUPPLEMENTARY MATERIAL

Supplementary Material is available at *HMG* online.

ACKNOWLEDGEMENTS

We are grateful to Hiroko Meguro for microarray experiment, Kaoru Nakano for MassARRAY analysis, Elodie Lebredonchel for bisulfite sequencing experiment and Michael Jones for critical reading of the manuscript.

Conflict of Interest statement. None declared.

FUNDING

This work was mainly supported by a Grant-in-Aid for Scientific Research (S) 20221009 (H.A.) from the Ministry of Education, Culture, Sports, Science and Technology (MEXT), Japan, and the Program of Fundamental Studies in Health Sciences of the National Institute of Biomedical Innovation (NIBIO), Japan.

REFERENCES

1. Bird, A. (2002) DNA methylation patterns and epigenetic memory. *Genes Dev.*, **16**, 6–21.
2. Bernstein, B.E., Meissner, A. and Lander, E.S. (2007) The mammalian epigenome. *Cell*, **128**, 669–681.
3. Li, E., Bestor, T.H. and Jaenisch, R. (1992) Targeted mutation of the DNA methyltransferase gene results in embryonic lethality. *Cell*, **69**, 915–926.
4. Okano, M., Bell, D.W., Haber, D.A. and Li, E. (1999) DNA methyltransferases Dnmt3a and Dnmt3b are essential for de novo methylation and mammalian development. *Cell*, **99**, 247–257.
5. Jackson-Grusby, L., Beard, C., Possemato, R., Tudor, M., Fambrough, D., Csankovszki, G., Dausman, J., Lee, P., Wilson, C., Lander, E. *et al.* (2001) Loss of genomic methylation causes p53-dependent apoptosis and epigenetic deregulation. *Nat. Genet.*, **27**, 31–39.
6. Rakyan, V.K., Down, T.A., Thorne, N.P., Flicek, P., Kulesha, E., Graf, S., Tomazou, E.M., Backdahl, L., Johnson, N., Herberth, M. *et al.* (2008) An integrated resource for genome-wide identification and analysis of human tissue-specific differentially methylated regions (tDMRs). *Genome Res.*, **18**, 1518–1529.
7. Khulan, B., Thompson, R.F., Ye, K., Fazzari, M.J., Suzuki, M., Stasiek, E., Figueroa, M.E., Glass, J.L., Chen, Q., Montagna, C. *et al.* (2006)

Comparative isoschizomer profiling of cytosine methylation: the HELP assay. *Genome Res.*, **16**, 1046–1055.
8. Shen, L., Kondo, Y., Guo, Y., Zhang, J., Zhang, L., Ahmed, S., Shu, J., Chen, X., Waterland, R.A. and Issa, J.P. (2007) Genome-wide profiling of DNA methylation reveals a class of normally methylated CpG island promoters. *PLoS Genet.*, **3**, 2023–2036.
9. Straussman, R., Nejman, D., Roberts, D., Steinfeld, I., Blum, B., Benvenisty, N., Simon, I., Yakhini, Z. and Cedar, H. (2009) Developmental programming of CpG island methylation profiles in the human genome. *Nat. Struct. Mol. Biol.*, **16**, 564–571.
10. Eckhardt, F., Lewin, J., Cortese, R., Rakyan, V.K., Attwood, J., Burger, M., Burton, J., Cox, T.V., Davies, R., Down, T.A. *et al.* (2006) DNA methylation profiling of human chromosomes 6, 20 and 22. *Nat. Genet.*, **38**, 1378–1385.
11. Illingworth, R., Kerr, A., DeSousa, D., Jorgensen, H., Ellis, P., Stalker, J., Jackson, D., Clee, C., Plumb, R., Rogers, J. *et al.* (2008) A novel CpG island set identifies tissue-specific methylation at developmental gene loci. *PLoS Biol.*, **6**, e22.
12. Laird, P.W. (2010) Principles and challenges of genome-wide DNA methylation analysis. *Nat. Rev. Genet.*, **11**, 191–203.
13. Waterland, R.A., Kellermayer, R., Rached, M.T., Tatevian, N., Gomes, M.V., Zhang, J., Zhang, L., Chakravarty, A., Zhu, W., Laritsky, E. *et al.* (2009) Epigenomic profiling indicates a role for DNA methylation in early postnatal liver development. *Hum. Mol. Genet.*, **18**, 3026–3038.
14. Saxonov, S., Berg, P. and Brutlag, D.L. (2006) A genome-wide analysis of CpG dinucleotides in the human genome distinguishes two distinct classes of promoters. *Proc. Natl Acad. Sci. USA*, **103**, 1412–1417.
15. Irizarry, R.A., Ladd-Acosta, C., Carvalho, B., Wu, H., Brandenburg, S.A., Jeddeloh, J.A., Wen, B. and Feinberg, A.P. (2008) Comprehensive high-throughput arrays for relative methylation (CHARM). *Genome Res.*, **18**, 780–790.
16. Barrera, L.O., Li, Z., Smith, A.D., Arden, K.C., Cavenee, W.K., Zhang, M.Q., Green, R.D. and Ren, B. (2008) Genome-wide mapping and analysis of active promoters in mouse embryonic stem cells and adult organs. *Genome Res.*, **18**, 46–59.
17. Bibikova, M., Le, J., Barnes, B., Saedinia-Melnyk, S., Zhou, L., Shen, R. and Gunderson, K.L. (2009) Genome-wide DNA methylation profiling using infinium assay. *Epigenomics*, **1**, 177–200.
18. Jones, P.A. and Takai, D. (2001) The role of DNA methylation in mammalian epigenetics. *Science*, **293**, 1068–1070.
19. Walsh, C.P. and Bestor, T.H. (1999) Cytosine methylation and mammalian development. *Genes Dev.*, **13**, 26–34.
20. Baek, D., Davis, C., Ewing, B., Gordon, D. and Green, P. (2007) Characterization and predictive discovery of evolutionarily conserved mammalian alternative promoters. *Genome Res.*, **17**, 145–155.
21. Kadonaga, J.T. (1998) Eukaryotic transcription: an interlaced network of transcription factors and chromatin-modifying machines. *Cell*, **92**, 307–313.
22. Yang, A., Zhu, Z., Kapranov, P., McKeon, F., Church, G.M., Gingeras, T.R. and Struhl, K. (2006) Relationships between p63 binding, DNA sequence, transcription activity, and biological function in human cells. *Mol. Cell*, **24**, 593–602.
23. Shiraki, N., Umeda, K., Sakashita, N., Takeya, M., Kume, K. and Kume, S. (2008) Differentiation of mouse and human embryonic stem cells into hepatic lineages. *Genes Cells*, **13**, 731–746.
24. Takahashi, K. and Yamanaka, S. (2006) Induction of pluripotent stem cells from mouse embryonic and adult fibroblast cultures by defined factors. *Cell*, **126**, 663–676.
25. Wernig, M., Meissner, A., Foreman, R., Brambrink, T., Ku, M., Hochedlinger, K., Bernstein, B.E. and Jaenisch, R. (2007) *In vitro* reprogramming of fibroblasts into a pluripotent ES-cell-like state. *Nature*, **448**, 318–324.
26. Cedar, H. and Bergman, Y. (2009) Linking DNA methylation and histone modification: patterns and paradigms. *Nat. Rev. Genet.*, **10**, 295–304.
27. Weber, M., Hellmann, I., Stadler, M.B., Ramos, L., Paabo, S., Rebhan, M. and Schubeler, D. (2007) Distribution, silencing potential and evolutionary impact of promoter DNA methylation in the human genome. *Nat. Genet.*, **39**, 457–466.
28. Reik, W. (2007) Stability and flexibility of epigenetic gene regulation in mammalian development. *Nature*, **447**, 425–432.
29. Bergman, Y. and Mostoslavsky, R. (1998) DNA demethylation: Turning genes on. *Biol. Chem.*, **379**, 401–407.
30. Eden, S. and Cedar, H. (1994) Role of DNA methylation in the regulation of transcription. *Curr. Opin. Genet. Dev.*, **4**, 255–259.
31. Ooi, S.K.T. and Bestor, T.H. (2008) The colorful history of active DNA demethylation. *Cell*, **133**, 1145–1148.
32. Wu, S.C. and Zhang, Y. (2010) Active DNA demethylation: many roads lead to Rome. *Nat. Rev. Mol. Cell Biol.*, **11**, 607–620.
33. Mayer, W., Niveleau, A., Walter, J., Fundele, R. and Haaf, T. (2000) Embryogenesis: demethylation of the zygotic paternal genome. *Nature*, **403**, 501–502.
34. Oswald, J., Engemann, S., Lane, N., Mayer, W., Olek, A., Fundele, R., Dean, W., Reik, W. and Walter, J. (2000) Active demethylation of the paternal genome in the mouse zygote. *Curr. Biol.*, **10**, 475–478.
35. Reik, W., Dean, W. and Walter, J. (2001) Epigenetic reprogramming in mammalian development. *Science*, **293**, 1089–1093.
36. Ito, S., D'Alessio, A.C., Taranova, O.V., Hong, K., Sowers, L.C. and Zhang, Y. (2010) Role of Tet proteins in 5mC to 5hmC conversion, ES-cell self-renewal and inner cell mass specification. *Nature*, **466**, 1129–1133.
37. Young, D.W., Hassan, M.Q., Yang, X.-Q., Galindo, M., Javed, A., Zaidi, S.K., Furcinitti, P., Lapointe, D., Montecino, M., Lian, J.B. *et al.* (2007) Mitotic retention of gene expression patterns by the cell fate-determining transcription factor Runx2. *Proc. Natl Acad. Sci. USA*, **104**, 3189–3194.
38. Zaidi, S.K., Young, D.W., Montecino, M.A., Lian, J.B., van Wijnen, A.J., Stein, J.L. and Stein, G.S. (2010) Mitotic bookmarking of genes: a novel dimension to epigenetic control. *Nat. Rev. Genet.*, **11**, 583–589.
39. Takahashi, K., Tanabe, K., Ohnuki, M., Narita, M., Ichisaka, T., Tomoda, K. and Yamanaka, S. (2007) Induction of pluripotent stem cells from adult human fibroblasts by defined factors. *Cell*, **131**, 861–872.
40. Vierbuchen, T., Ostermeier, A., Pang, Z.P., Kokubu, Y., Sudhof, T.C. and Wernig, M. (2010) Direct conversion of fibroblasts to functional neurons by defined factors. *Nature*, **463**, 1035–1041.
41. Ieda, M., Fu, J.-D., Delgado-Olguin, P., Vedantham, V., Hayashi, Y., Bruneau, B.G. and Srivastava, D. (2010) Direct reprogramming of fibroblasts into functional cardiomyocytes by defined factors. *Cell*, **142**, 375–386.
42. Suemori, H., Yasuchika, K., Hasegawa, K., Fujioka, T., Tsuneyoshi, N. and Nakatsuji, N. (2006) Efficient establishment of human embryonic stem cell lines and long-term maintenance with stable karyotype by enzymatic bulk passage. *Biochem. Biophys. Res. Commun.*, **345**, 926–932.
43. D'Amour, K.A., Agulnick, A.D., Eliazer, S., Kelly, O.G., Kroon, E. and Baetge, E.E. (2005) Efficient differentiation of human embryonic stem cells to definitive endoderm. *Nat. Biotech.*, **23**, 1534–1541.
44. Hayashi, H., Nagae, G., Tsutsumi, S., Kaneshiro, K., Kozaki, T., Kaneda, A., Sugisaki, H. and Aburatani, H. (2007) High-resolution mapping of DNA methylation in human genome using oligonucleotide tiling array. *Hum. Genet.*, **120**, 701–711.
45. Hippo, Y., Watanabe, K., Watanabe, A., Midorikawa, Y., Yamamoto, S., Ihara, S., Tokita, S., Iwanari, H., Ito, Y., Nakano, K. *et al.* (2004) Identification of soluble NH2-terminal fragment of glypican-3 as a serological marker for early-stage hepatocellular carcinoma. *Cancer Res.*, **64**, 2418–2423.
46. Shiraki, N., Yoshida, T., Araki, K., Umezawa, A., Higuchi, Y., Goto, H., Kume, K. and Kume, S. (2008) Guided differentiation of embryonic stem cells into Pdx1-expressing regional-specific definitive endoderm. *Stem Cells*, **26**, 874–885.
47. Eisen, M.B., Spellman, P.T., Brown, P.O. and Botstein, D. (1998) Cluster analysis and display of genome-wide expression patterns. *Proc. Natl Acad. Sci. USA*, **95**, 14863–14868.
48. Saldanha, A.J. (2004) Java Treeview–extensible visualization of microarray data. *Bioinformatics*, **20**, 3246–3248.

Carcinogenesis vol.32 no.11 pp.1597–1606, 2011
doi:10.1093/carcin/bgr183
Advance Access publication August 8, 2011

Transient depletion of p53 followed by transduction of c-Myc and K-Ras converts ovarian stem-like cells into tumor-initiating cells

Takeshi Motohara[1,2], Sachiko Masuko[1], Takatsugu Ishimoto[1], Toshifumi Yae[1], Nobuyuki Onishi[1], Teruyuki Muraguchi[3], Atsushi Hirao[3], Yumi Matsuzaki[4], Hironori Tashiro[2], Hidetaka Katabuchi[2], Hideyuki Saya[1,5] and Osamu Nagano[1,5,*]

[1]Division of Gene Regulation, Institute for Advanced Medical Research, School of Medicine, Keio University, 35 Shinanomachi, Shinjuku-ku, Tokyo 160-8582, Japan, [2]Department of Obstetrics and Gynecology, Faculty of Life Sciences, Kumamoto University, Honjo 1-1-1, Kumamoto City, Kumamoto 860-8556, Japan, [3]Division of Molecular Genetics, Center for Cancer and Stem Cell Research, Cancer Research Institute, Kanazawa University, Kanazawa, Ishikawa 920-0934, Japan, [4]Department of Physiology, Keio University School of Medicine, Tokyo, Japan and [5]Core Research for Evolutional Science and Technology (CREST), Japan Science and Technology Agency, Tokyo, Japan.

*To whom correspondence should be addressed. Tel: +81 3 5363 3983; Fax: +81 3 5363 3982;
Email: osmna@sb3.so-net.ne.jp

Although the existence of tumor-initiating cells (T-ICs) in several types of human cancer has been documented, the contribution of somatic stem cells to the development of T-ICs has remained unclear. Here, we show that normal mouse ovary contains epithelial cell adhesion molecule (EpCAM)-expressing stem-like cells that possess the ability to differentiate into cytokeratin 8 (CK8)-expressing epithelial progeny cells. Furthermore, RNA interference-mediated transient depletion of the tumor suppressor p53 followed by retrovirus-mediated transfer of c-Myc and K-Ras oncogenes in EpCAM-expressing ovarian stem-like cells resulted in the generation of ovarian T-ICs. The established ovarian T-ICs gave rise to hierarchically organized lethal tumors *in vivo* and were able to undergo peritoneal metastasis. Finally, subsequent RNA interference-mediated knockdown of p53 in tumor cells triggered the expansion of EpCAM-expressing stem-like tumor cells and induced further tumor growth. These data reveal a role for p53 in the development and expansion of ovarian stem-like tumor cells and subsequent malignant progression.

Introduction

Ovarian cancer is the leading cause of death from gynecological malignancies. The clinical outcome of women with advanced ovarian cancer is poor even after treatment with aggressive surgery and intensive chemotherapy. Even though the cancer may respond to primary therapy, most tumors undergo relapse in the peritoneal cavity that is associated with chemoresistant residual cells (1). Although human ovarian tumor-initiating cells (T-ICs) have not been fully characterized, such stem-like cancer cells are thought to play a key role in chemoresistance and relapse of cancer. Improved targeted gene therapies and chemosensitization strategies are therefore needed to eradicate T-ICs in ovarian cancer. Ovarian cancer research has been hampered, however, by a lack of appropriate model systems with which to investigate the molecular mechanisms of tumor initiation and progression in relation to the biology of somatic stem cells and T-ICs.

Abbreviations: CK8, cytokeratin 8; CSC, cancer stem cell; DMEM, Dulbecco's modified Eagle's medium; EpCAM, epithelial cell adhesion molecule; GFP, green fluorescent protein; KuO, Kusabira Orange; mRNA, messenger RNA; OSE, ovarian surface epithelium; PCR, polymerase chain reaction; RT, reverse transcription; siRNA, small interfering RNA; TBS, Tris-buffered saline; T-IC, tumor-initiating cell.

Evidence suggests that human cancers are derived from somatic stem cells and are composed of hierarchies of cells sustained by T-ICs (2,3). Whereas most ovarian epithelial cancers are thought to arise from the ovarian surface epithelium (OSE) (4,5), the cells of origin for such tumors have remained obscure (6,7). The identification of cell surface markers common to ovarian epithelial stem cells and T-ICs may provide insight into the origin of T-ICs.

Epithelial cell adhesion molecule (EpCAM) (8,9), also known as epithelial-specific antigen, is a type I transmembrane glycoprotein that is expressed specifically in epithelial tissues and is overexpressed in some epithelial cancers (10,11). In normal tissues, EpCAM is expressed in several types of epithelial stem/progenitor cells and contributes to tissue development (12–14). On the other hand, a subpopulation of EpCAM-positive ($EpCAM^{POS}$) cells has been identified as T-ICs in human colon (15), breast (16), liver (17) and pancreatic (18) cancers. In addition, increased EpCAM expression in human ovarian cancer has been associated with poor clinical outcome (19). Those data suggest the possibility that EpCAM is a common marker for epithelial cells and T-ICs in ovarian tissue.

Genetic alterations of oncogenes and tumor suppressor genes have been implicated in ovarian cancer formation and progression (1). Proto-oncogenes such as those for c-Myc and K-Ras are often amplified, overexpressed or mutated in ovarian epithelial cancer (1,20,21), whereas dysfunction of signaling by the tumor suppressor p53 pathway has been identified as the most common defect in high-grade serous or undifferentiated adenocarcinoma of the ovary (22,23). Whether p53 dysfunction plays a role in the generation or affects the behavior of ovarian T-ICs has remained unknown, however. Investigation of the roles of p53 signaling in T-ICs and in their precursor cells will require the establishment of appropriate ovarian cancer models.

In the present study, we identify a subpopulation of $EpCAM^{POS}$ cells as candidate ovarian epithelial stem-like cells and we were able to generate ovarian T-ICs from these cells. We also found that $EpCAM^{POS}$ cells isolated from hierarchically organized ovarian tumors possess cancer stem cell (CSC) traits and are regulated by p53.

Materials and methods

Mice

C57BL/6 mice were obtained from CLEA Japan and were bred and maintained according to institutional guidelines. All animal experiments were performed in accordance with protocols approved by the animal ethics committee of Keio University.

Cell preparation

Ovarian tissues were surgically isolated from 7-week-old C57BL/6 mice and dissociated by incubation for 3–4 h at 37°C with collagenase (300 U/ml) and hyaluronidase (100 U/ml). Red blood cells in the tissue digest were lysed by exposure to NH_4Cl. A single-cell suspension was obtained by sequential dissociation of the remaining tissue fragments by gentle pipetting in the presence of dispase (5 mg/ml) and DNase (0.1 mg/ml) followed by filtration through a 40 μm nylon mesh. All reagents were from STEMCELL Technologies (Vancouver, Canada).

Flow cytometry

Cell sorting and flow cytometric analysis were performed with the use of a FACSAria Cell Sorter (BD Biosciences, Tokyo, Japan) or Moflo flow cytometer (DakoCytomation, Glostrup, Denmark). Cells were incubated with antibodies for 15 min. APC-conjugated antibody to EpCAM (G8.8) and pacific blue-conjugated antibodies to CD44 and to CD117 were obtained from BioLegend (San Diego, CA). Sorted cells were maintained in Dulbecco's modified Eagle's medium (DMEM)-F12 (Sigma, St Louis, MO) supplemented with 10% FBS for further analysis.

Small interfering RNA transfection

The sequences of small interfering RNA (siRNA, chimeric RNA–DNA) duplexes (Japan Bioservice, Saitama, Japan) were 5′-GUACUCUCCUCCCCUCAAUTT-3′ and 5′-AUUGAGGGGAGGAGAGUACTT-3′ for p53 siRNA and 5′-CGUACGCGGAAUACUUCGATT-3′ and 5′-UCGAAGUAUUCCGCGUACGTT-3′ for luciferase siRNA (GL-2, control). Cells were transfected with the annealed siRNAs for 72 h in the presence of Lipofectamine RNAi MAX reagent (Invitrogen, Tokyo, Japan).

Mouse ovarian tumor model

$EpCAM^{POS}$ cells in the ovaries of 7-week-old mice were isolated by FACS and were transfected with p53 siRNA in adherent cultures. Retroviruses encoding human c-Myc or $K\text{-}Ras^{G12V}$ were generated by transfection of Plat-E-packaging cells with the retroviral vectors pMXs-c-Myc-IRES-enhanced green fluorescent protein (GFP) (24) or pGCDN-$K\text{-}Ras^{G12V}$-IRES-Kusabira Orange (KuO) (25) with the use of the FuGENE HD transfection reagent (Roche, Mannheim, Germany). The isolated retroviruses were then used to infect sorted $EpCAM^{POS}$ cells in floating culture. The cells were then transplanted in 50 μl of DMEM-F12 into the left ovarian bursa of 7-week-old syngeneic recipient mice.

Transplantation assays

Sorted tumor-derived cells were suspended in DMEM-F12 and injected orthotopically, intraperitoneally or subcutaneously into 7-week-old syngeneic female C57BL/6 mice. T-IC frequencies were estimated with the use of ELDA software for limiting dilution analysis (26).

Histology and immunofluorescence analysis

Tissue was fixed in 10% buffered formalin, embedded in paraffin and sectioned at a thickness of 4 μm. Sections were stained with hematoxylin and eosin for histological analysis. For immunofluorescence staining, tissue sections were incubated at room temperature for 30 min with Tris-buffered saline (TBS) containing 0.2% Triton X-100 and for 60 min with TBS containing 3% bovine serum albumin before exposure overnight at 4°C to primary antibodies diluted in TBS containing 1.5% bovine serum albumin. The sections were then incubated with Alexa Fluor 488- or Texas red-conjugated secondary antibodies (Invitrogen, Carlsbad, CA) diluted in TBS containing 0.2% bovine serum albumin and were mounted in Vectashield mounting medium containing 4′,6-diamidino-2-phenylindole (Vector Laboratories, Burlingame, CA). Cultured cells were fixed with 4% paraformaldehyde and incubated at room temperature for 60 min with primary antibodies, for 60 min with appropriate secondary antibodies and for 5 min with Hoechst 33342 (Invitrogen) for detection of nuclei. Sections and cells were viewed with a Biorevo BZ-9000 fluorescence microscope (Keyence, Tokyo, Japan). EpCAM was detected with the rat monoclonal antibody G8.8 (Santa Cruz Biotechnology, Santa cruz, CA), cytokeratin 8 (CK8) was detected with rabbit polyclonal antibodies (Abcam, Cambridge, UK), and CA125 was detected with rabbit polyclonal antibodies (Abbiotec, San Diego, CA).

In vivo fluorescence imaging

Twenty-four hours before tumor imaging, mice were injected intravenously with 2 nmol of IntegriSense 750 (VisEn Medical, Bedford, MA). Imaging was performed with the use of an *in vivo* fluorescence imager ClairvivoOPT (Shimadzu Corporation, Kyoto, Japan) with a 785 nm laser diode for excitation and an 845/855 nm band-pass filter for detection of IntegriSense 750 fluorescence. For quantitative comparisons, the total fluorescence signal intensities in the region of interest corresponding to each tumor were determined.

Sphere-forming assay

Sorted $EpCAM^{POS}$ cells or tumor-derived cells were seeded in low-attachment plates and grown in serum-free DMEM-F12 supplemented with 20 ng/ml epidermal growth factor, 10 ng/ml basic fibroblast growth factor (Peprotech, Rocky Hill, NJ) and B27 (1:50; Gibco, Karlsruhe, Germany). The number of spheres generated by sorted normal $EpCAM^{POS}$ cells or tumor-derived cells were counted after 7 or 5 days, respectively.

reverse transcription–polymerase chain reaction analysis

Total RNA was extracted from sorted $EpCAM^{POS}$ cells or primary tumor-derived cells with the use of Isogen (Nippon Gene, Tokyo, Japan) and was subjected to reverse transcription (RT)–polymerase chain reaction (PCR) analysis with specific primers; *GAPDH* messenger RNA (mRNA) was examined as an internal control. Quantitative RT–PCR analysis was performed with the use of the Thermal Cycler Dice Real Time System (Takara Bio, Tokyo, Japan). The amplification protocol comprised an initial incubation at 95°C for 2 min, 40 cycles of 95°C for 30 s and 60°C for 30 s, followed by dissociation curve analysis to confirm specificity. Primer sets for RT–PCR analysis (forward and reverse, respectively) were as follows: *p53*, 5′-GCCAAGTCTGTTATGTGCAC-3′ and 5′-GCTGTGACTTCTTGTAGATG-3′; *MUC16*, 5′-TGCCACCTACCAGTTGAAAG-3′ and 5′-GTACCGCCAAGCAGATGAG-3′; *EpCAM*, 5′-AGACTGTGTCTGTGACAACTACAAG-3′ and 5′-GTCATTTCTGCTTTCATCGCCAA-3′; *CD44*, 5′-AATTCCGAGGATTCATCCCA-3′ and 5′-CGCTGCTGACATCGTCATC-3′; *CD117*, 5′-GACGCAACTTCCTTATGATC-3′ and 5′-TGGTTTGAGCATCTTCACGG-3′; *Snail*, 5′-GCCGGAAGCCCAACTATAGCGA-3′ and 5′-AGATGAGGGCAGCG-3′; *Slug*, 5′-ATCGTCGGCAGCTCCACT-3′ and 5′-GTCACTAATGGGACTTTCTGAACCACT-3′; *Twist*, 5′-CGGGTCATGGCTAACGTG-3′ and 5′-CAGCTTGCCATCTTGGAGTC-3′ and *GAPDH*, 5′-GTGAAGGTCGGTGTGAACG-3′ and 5′-GACCATGTAGTTGAGGTCAATG-3′ (quantitative RT–PCR), 5′-GTGAAGGTCG GTGTGAACG-3′ and 5′-CTCACCCCATTTGATGTTAGTG-3′ (semiquantitative RT–PCR).

Establishment of mouse ovarian tumor cell lines expressing human EpCAM protein

The full-length human EpCAM (hEpCAM) complementary DNA was amplified by PCR from the complementary DNA of HCT116 cells by the following primers: EpCAM-sense (5′-CCGCTCGAGATGGCGCCCCCGCAGGTCC-3′) containing an XhoI site (underlined) and EpCAM-antisense (5′-ATAAGAATGCGGCCGCTTATGCATTGAGTTC-3′) containing a NotI site (underlined). The PCR fragments were digested with XhoI and NotI and then ligated into pMXs-IG expression plasmids (27). Retroviral gene transfer into $EpCAM^{NEG}$ tumor cells was performed as described previously (24). hEpCAM-expressing cells were sorted with APC-conjugated antibodies to human EpCAM (Miltenyi Biotec, Auburn, CA) using Moflo flow cytometer.

Immunoblot analysis

Immunoblot analysis was performed as described previously (28). In brief, equal amounts of cell lysate protein were subjected to sodium dodecyl sulfate–polyacrylamide gel electrophoresis, transferred to a nitrocellulose membrane and exposed to anti-EpCAM antibody (R&D systems, Minneapolis, MN). Immune complexes were detected with Chemiluminescence Reagent Plus (PerkinElmer Japan, Yokohama, Japan).

Matrigel invasion assay

BD BioCoat Matrigel Invasion Chambers (BD Biosciences, Bedford, MA) were used in accordance with the manufacturer's instructions. Established mouse ovarian tumor cells (5×10^4) in serum-free DMEM-F12 were seeded onto Matrigel-coated filters in the upper chambers. In the lower chambers, DMEM-F12 containing 10% FBS was added as a chemoattractant. After 24 h of incubation, cells on the upper surface of the filters were removed with a cotton swab, and the filters were fixed with 100% methanol and stained with Diff-Quik. The invasive ability of the tumor cells was expressed as the mean number of cells in three fields.

Statistical analysis

Data are presented as means ± SDs and were analyzed with the unpaired Student's *t*-test. A P value of <0.05 was considered statistically significant.

Results

EpCAM as a potential marker for epithelial stem-like cells in adult mouse ovary and expansion of ovarian stem-like cells induced by p53 depletion in vitro

The identity of epithelial stem cells responsible for the maintenance and regenerative repair of the adult ovarian epithelium has remained unclear. Given that EpCAM is a marker of several types of stem cell (13,14,29), we examined the expression of EpCAM in the normal mouse ovary. Immunohistofluorescence analysis revealed that most $EpCAM^{POS}$ cells were located near the OSE, a single layer of cells that covers the surface of the ovary, as well as in the ovarian medulla near blood vessels (Figure 1A). EpCAM expression was largely undetectable in OSE cells, which express CK 8 at a high level (Figure 1A), suggesting that $EpCAM^{POS}$ ovarian cells are distinct from differentiated epithelial cells of the OSE. Flow cytometric analysis with antibodies to EpCAM revealed that the frequency of $EpCAM^{POS}$ cells in the adult ovary ranged from 2.9 to 3.9% of total cells (mean of 3.6%) (Figure 1B). For examination of the differentiation capacity of $EpCAM^{POS}$ cells, sorted $EpCAM^{POS}$ cells were cultured on Matrigel, a reconstituted basement membrane, for 10 days. Individual $EpCAM^{POS}$ cells formed multicellular spherical structures consisting of $EpCAM^{POS}CK8^{POS}$ and OSE-like $EpCAM^{NEG}CK8^{POS}$

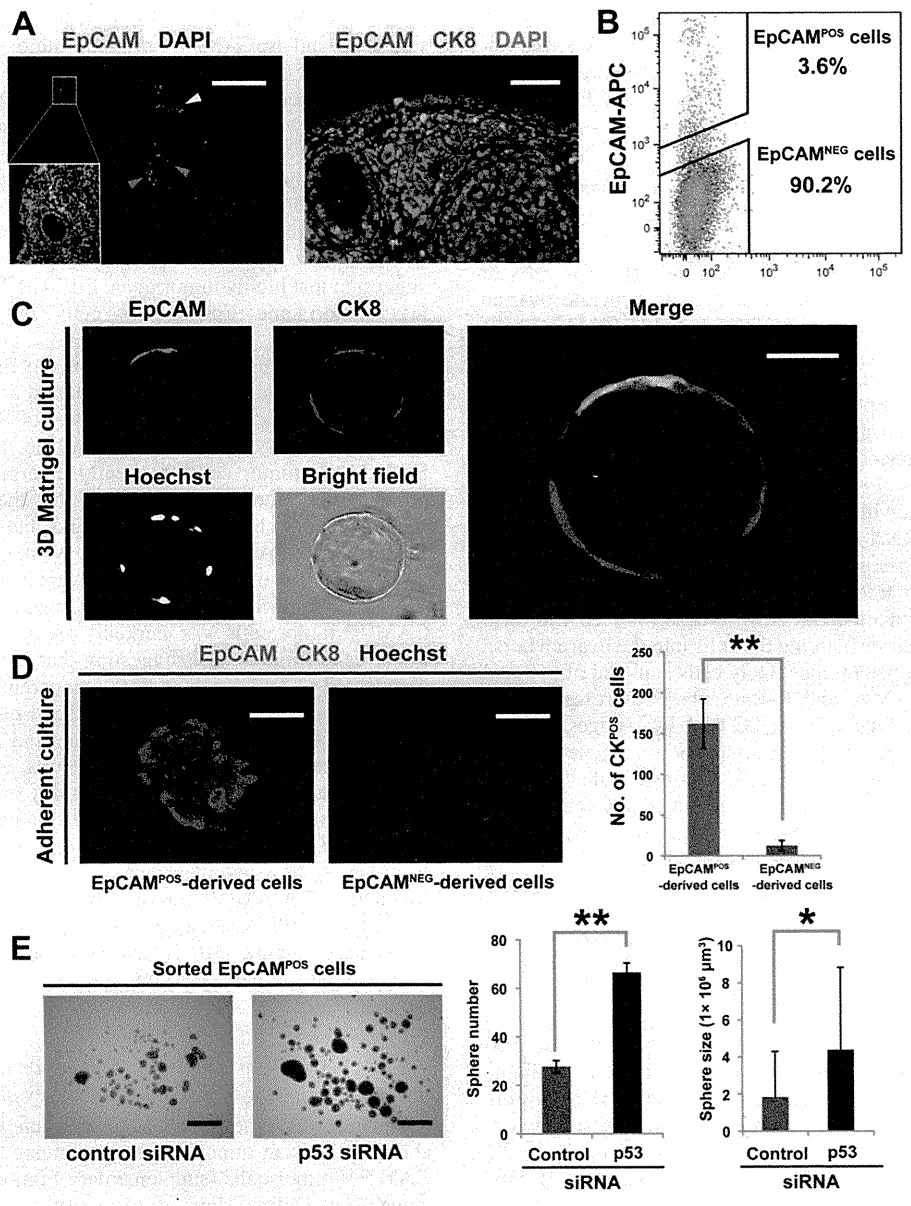

Fig. 1. EpCAM as a candidate marker for epithelial stem or progenitor cells in the normal mouse ovary and expansion of stem-like cells induced by p53 depletion. (**A**) Paraffin-embedded sections of normal mouse ovary were subjected to immunofluorescence analysis with antibodies to EpCAM (G8.8) and to CK8. Nuclei were stained with 4′,6-diamidino-2-phenylindole. Most $EpCAM^{POS}$ cells were localized near the OSE (white arrowhead) and in the ovarian medulla (gray arrowheads). Scale bars: 500 μm (left panel) or 50 μm (right panel). (**B**) Flow cytometric analysis of mouse ovarian cells with APC-conjugated antibodies to EpCAM. (**C**) Sorted $EpCAM^{POS}$ cells were grown in 3D Matrigel culture for 10 days, and the resulting single cell-derived colonies were then subjected to immunofluorescence analysis with antibodies to EpCAM and to CK8. Nuclei were stained with Hoechst 33342. Scale bar, 50 μm. (**D**) Sorted $EpCAM^{POS}$ or $EpCAM^{NEG}$ cells (5×10^3) were cultured in the presence of 10% FBS under adherent conditions for 3 days and then subjected to immunofluorescence analysis as in (**C**). Scale bars: 50 μm (left image) or 100 μm (right image). The numbers of $CK8^{POS}$ cells derived from the $EpCAM^{POS}$ or $EpCAM^{NEG}$ cells were determined as means ± SDs from three independent experiments $^{**}P < 0.01$. (**E**) Sorted $EpCAM^{POS}$ cells transfected with p53 or control siRNAs were seeded in low-attachment plates (5×10^4 cells per well) and cultured in serum-free medium supplemented with epidermal growth factor, basic fibroblast growth factor and B27. The spheres formed by the cells were photographed (scale bars, 500 μm), and the number and size of spheres were determined as means ± SDs from three independent experiments. $^{*}P < 0.05$, $^{**}P < 0.01$.

cells (Figure 1C), whereas $EpCAM^{NEG}$ cells failed to form $CK8^{POS}$ spherical cysts. These results thus suggested that $EpCAM^{POS}$ ovarian cells are able to form an OSE-like structure composed by $EpCAM^{NEG}CK8^{POS}$ cells on reconstituted basement membrane. Furthermore, culture of sorted $EpCAM^{POS}$ or $EpCAM^{NEG}$ cells in culture dishes in the presence of FBS revealed that EpCAM expression was downregulated in adherent cells and that more $CK8^{POS}$ cells were derived from $EpCAM^{POS}$ cells than from $EpCAM^{NEG}$ cells (Figure 1D), suggesting that the $EpCAM^{POS}$ cell population might contain epithelial stem or progenitor cells that give rise to the OSE. To test this hypothesis, we examined whether the $EpCAM^{POS}$ cell population contains stem-like cells with sphere-forming ability. Sorted $EpCAM^{POS}$ cells seeded on low-attachment plates in serum-free medium supplemented with epidermal growth factor, basic fibroblast growth factor and B27 formed non-adherent spherical clusters of cells within several days after plating (Figure 1E), suggesting that $EpCAM^{POS}$ cells indeed include stem-like cells that possess sphere-forming ability.

Given that loss of p53 expression increases the size of stem cell populations (30), we examined the effect of RNA interference-mediated depletion of p53 (supplementary Figure 1 is available at *Carcinogenesis* Online) on sphere formation by sorted $EpCAM^{POS}$ cells.

EpCAM^{POS} cells transfected with a siRNA specific for p53 mRNA yielded more and larger spheres under non-adherent conditions compared with those transfected with a control siRNA (Figure 1E). This result thus suggested that p53 controls the expansion of EpCAM^{POS} epithelial stem-like cells.

Transient suppression of p53 followed by retroviral transduction of oncogenes in EpCAM^{POS} cells generates stem-like tumor cells that give rise to lethal ovarian tumors

Normal stem cells and progenitor cells are candidates for cells of origin of T-ICs (2,31). We therefore attempted to generate ovarian T-ICs by the introduction of oncogenes into sorted EpCAM^{POS} cells with a retroviral gene delivery system. Given that knockdown of p53 induced expansion of stem-like cells in the EpCAM^{POS} population, we transfected the sorted EpCAM^{POS} cells with p53 siRNA before their infection with a retrovirus encoding c-Myc plus GFP as a marker (24) or with a retrovirus encoding the K-Ras^{G12V} mutant plus humanized KuO as a marker (25) (Figure 2A). Immunofluorescence analysis revealed that the efficiency of retroviral infection was higher in cells transfected with p53 siRNA than in those transfected with control siRNA (Figure 2B), suggesting that p53 ablation increased the rate of retroviral infection in EpCAM^{POS} cells. We next examined the ability of the retrovirus-infected EpCAM^{POS} cells (5×10^4) to form ovarian tumors *in vivo* by transplanting the cells into the ovarian bursa of syngeneic immunocompetent mice. Only cells depleted of p53 and infected with both the c-Myc and K-Ras^{G12V} retroviruses formed lethal ovarian tumors *in vivo* (Figure 2C and D), suggesting that suppression of p53 expression is essential for oncogene-induced transformation of sorted EpCAM^{POS} cells. The established ovarian tumors spread from the ovary to the intraperitoneal and retroperitoneal organs, resulting in massive abdominal distension by hemorrhagic ascites, within 4–5weeks after transplantation (Figure 2E). These results thus suggested that transient knockdown of p53 together with forced expression of both c-Myc and K-Ras^{G12V} was able to transform EpCAM^{POS} cells isolated from adult mouse ovary.

To examine the characteristics of cells derived from the primary ovarian tumors, we sorted tumor cells positive for both GFP and KuO (supplementary Figure 2A is available at *Carcinogenesis* Online) and assayed these cells for sphere-forming ability. The tumor-derived cells indeed formed spheres (supplementary Figure 2B is available at *Carcinogenesis* Online), with cells of these spheres also forming new spheres on serial passage *in vitro*, and they gave rise to histologically similar tumors on serial allograft passage *in vivo* (Figure 2F, supplementary Figure 2C, available at *Carcinogenesis* Online). Furthermore, Matrigel invasion analysis revealed that tumor-derived cells show highly invasive character when cells were incubated in FBS-containing medium (supplementary Figure 2D is available at *Carcinogenesis* Online). Thus, the established ovarian tumors contain stem-like tumor cells and invasive tumor cells.

The established ovarian tumors expressed CA125 (supplementary Figure 2E is available at *Carcinogenesis* Online), which is a marker of human ovarian epithelial cancer (1) and CK8 (supplementary Figure 2F is available at *Carcinogenesis* Online). RT–PCR analysis also revealed that the abundance of *MUC16* (CA125) mRNA was increased in primary tumor-derived cells compared with normal EpCAM^{POS} cells (Figure 2G), indicating that an increase in MUC16 gene expression is associated with ovarian epithelial tumorigenesis in this model. We confirmed that the p53 gene was not mutated in the established ovarian tumor cells by DNA sequence analysis.

Established mouse ovarian tumors harbor EpCAM^{POS} stem-like tumor cells

To investigate whether the established mouse ovarian tumors are organized as hierarchies of cells sustained by T-ICs, we subjected tumor-derived cells to flow cytometric analysis with antibodies to EpCAM. EpCAM^{POS} tumor cells constituted 5.3–13.8% (mean of 10.4%) of the GFP and KuO double-positive cell population of primary ovarian tumors (Figure 3A). To compare the tumorigenic potential of EpCAM^{POS} and EpCAM^{NEG} tumor cells, we sorted EpCAM^{POS} and EpCAM^{NEG} primary tumor cells and serially transplanted them orthotopically into syngeneic mice. EpCAM^{POS} tumor cells developed secondary ovarian tumors at a frequency of 83.3% (five of six) with as few as 10 cells. In contrast, $\geq$500 EpCAM^{NEG} tumor cells were necessary to initiate lethal ovarian tumor formation (Table I, supplementary Figure 3A is available at *Carcinogenesis* Online). Furthermore, secondary ovarian tumors generated by EpCAM^{POS} primary tumor cells contained a percentage of EpCAM^{POS} cells similar to that apparent for primary tumors (Figure 3A). These results suggested that highly tumorigenic EpCAM^{POS} tumor cells give rise to less tumorigenic EpCAM^{NEG} cells *in vivo*, possibly through differentiation.

To examine further the change in the EpCAM^{POS} population in primary tumor-derived cells, we cultured sorted EpCAM^{NEG} or EpCAM^{POS} tumor cells *in vitro* for 2 weeks. Although only a few EpCAM^{POS} tumor cells arose from the EpCAM^{NEG} population, EpCAM^{NEG} tumor cells frequently emerged from the EpCAM^{POS} population (Figure 3A), suggesting that the established ovarian tumors are hierarchically organized and that EpCAM^{POS} tumor cells give rise to EpCAM^{NEG} tumor cells. We next investigated the sphere-forming ability of EpCAM^{POS} and EpCAM^{NEG} tumor cells sorted from primary ovarian tumors. The sphere-forming activity of EpCAM^{POS} tumor cells was markedly greater than that of EpCAM^{NEG} tumor cells (Figure 3B), suggesting that EpCAM^{POS} tumor cells are maintained in an immature state compared with EpCAM^{NEG} tumor cells. Together, these data showed that EpCAM^{POS} tumor cells are highly efficient at tumor initiation and possess the ability to differentiate into EpCAM^{NEG} tumor cells.

Given that EpCAM^{POS} cells in primary ovarian tumors showed the characteristics of T-ICs, we next investigated the expression of CD44 and CD117, which were reported to be markers of human ovarian T-ICs (32), by flow cytometric analysis and quantitative RT–PCR. We found that EpCAM^{POS} tumor cells manifested high expression of CD44 and CD117 compared with EpCAM^{NEG} cells (Figure 3C, supplementary Figure 3B is available at *Carcinogenesis* Online), suggesting that these are common markers for human and mouse ovarian T-ICs.

EpCAM expression enhances the tumor-initiating ability and is regulated by c-Myc and K-Ras oncogenes in ovarian stem-like cells

To examine whether EpCAM expression impacts tumor-initiating ability of ovarian tumor cells, we expressed human EpCAM in EpCAM^{NEG} tumor cells (supplementary Figure 3C is available at *Carcinogenesis* Online). Forced expression of EpCAM enhanced tumor initiation ability in less tumorigenic EpCAM^{NEG} cells (Table I), suggesting that EpCAM expression plays a role in ovarian tumor formation.

To elucidate the mechanism underlining both c-Myc and K-Ras^{G12V}-induced conversion of ovarian stem-like cells, we next investigated the expression of *EpCAM* mRNA in ovarian stem-like cells transduced with c-Myc and K-Ras^{G12V}. Transduction of both c-Myc and K-Ras^{G12V} maintained high expression of EpCAM in ovarian stem-like cells compared with transduction of c-Myc or K-Ras^{G12V} alone (supplementary Figure 3D is available at *Carcinogenesis* Online). These results suggested that c-Myc and K-Ras^{G12V} oncogenes co-operatively induce EpCAM expression leading to the promotion of tumor-forming ability in ovarian tumor cells.

EpCAM^{POS} stem-like tumor cells have a high potential for peritoneal metastasis

Given that a key clinical characteristic of human ovarian cancer is its capacity for peritoneal metastasis, we next attempted to generate a mouse model of such metastasis by intraperitoneal injection of established ovarian T-ICs. IntegriSense *in vivo* imaging, which is able to detect integrin $\alpha v\beta 3$ expressing newly sprouting vasculature in tumor and thereby quantify tumor size, revealed that primary tumor-derived EpCAM^{POS} cells generated extensive disseminated tumors within

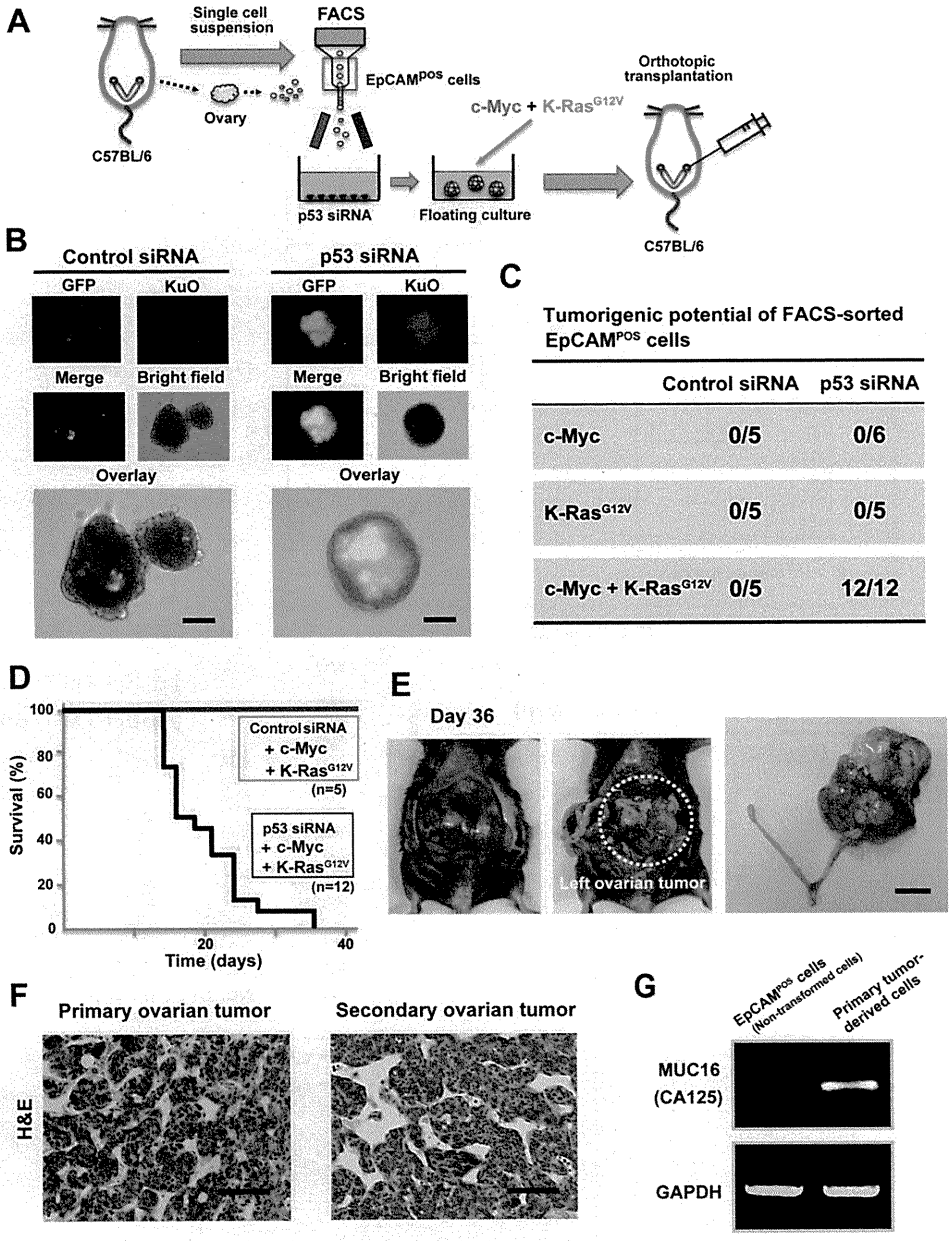

Fig. 2. Generation of ovarian T-ICs by transient knockdown of p53 and retroviral transduction of oncogenes in sorted EpCAM^{POS} cells. (**A**) Generation of an ovarian tumor model. EpCAM^{POS} ovarian cells were isolated by FACS, maintained in adherent culture for transfection with p53 siRNA and transferred to floating culture for retroviral transduction of c-Myc and K-Ras^{G12V} genes individually or in combination. The cells were then transplanted into the left ovarian bursa of syngeneic recipient mice. (**B**) The efficiency of sorted EpCAM^{POS} cell infection with retroviruses encoding c-Myc (plus GFP) and K-Ras^{G12V} (plus KuO) was examined by immunofluorescence analysis. The cells were transfected with control or p53 siRNAs before infection. Scale bars, 200 μm. (**C**) Summary of the tumorigenic potential of sorted EpCAM^{POS} cells transfected with control or p53 siRNAs and infected with retroviruses encoding c-Myc or K-Ras^{G12V} individually or in combination. The incidence of tumor formation within 8 weeks of cell transplantation (5×10^4 cells) was scored. Data represent the number of tumors per number of injections. (**D**) Survival curves for recipient mice transplanted with 5×10^4 c-Myc/K-Ras^{G12V}-expressing EpCAM^{POS} cells transfected with p53 siRNA (blue, $n = 12$) and that with control siRNA (gray, $n = 5$). (**E**) Macroscopic appearance of an ovarian tumor at 36 days after cell transplantation. The tumor spread from the ovary to the intraperitoneal and retroperitoneal organs, resulting in massive abdominal distension by hemorrhagic ascites. Tumors were macroscopically solid and cystic with the cysts containing bloody fluid. Scale bar, 2 cm. (**F**) Histopathology of primary and secondary ovarian tumors. Hematoxylin and eosin (H&E) staining revealed that the tumors consisted mostly of undifferentiated epithelial cells, resembling human poorly differentiated adenocarcinoma of the ovary. Nuclear pleomorphism and mitotic activity were prominent. Scale bars, 100 μm. (**G**) RT–PCR analysis of *MUC16* (CA125) mRNA in equal amounts of total RNA isolated from sorted EpCAM^{POS} cells (non-transformed) and primary tumor-derived cells. The mRNA for GAPDH was examined as an internal control.

2 weeks of injection (Figure 4A). In contrast, primary tumor-derived EpCAM^{NEG} cells showed little ability to form disseminated tumors in the peritoneal cavity (Figure 4A). Consistent with the results obtained with the IntegriSense *in vivo* imaging system, the total weight of disseminated tumors generated by EpCAM^{POS} tumor cells was significantly higher than that of those generated by EpCAM^{NEG} tumor cells (Figure 4B). Furthermore, these disseminated tumors invaded intraperitoneal and retroperitoneal organs including the omentum, intestine and kidneys (Figure 4C). Together, these observations suggested that EpCAM^{POS} tumor cells, but not EpCAM^{NEG} tumor cells, play a key role in peritoneal dissemination. Transplantation of EpCAM^{POS} T-ICs combined with the use of a non-invasive and quantitative fluorescence imaging system thus proves a useful model for the study of peritoneal metastasis.

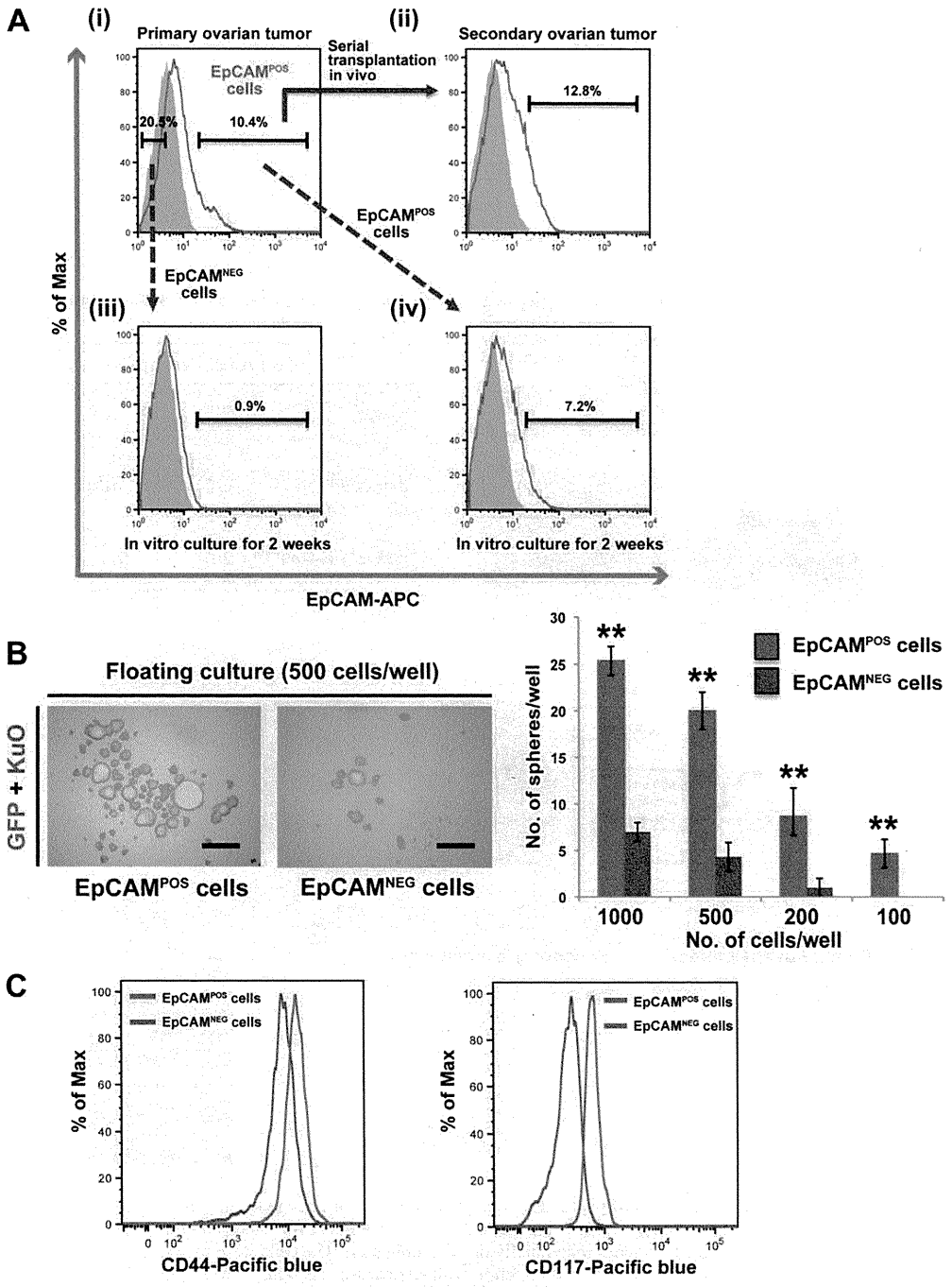

Fig. 3. Established mouse ovarian tumors contain EpCAM^{POS} stem-like tumor cells. (**A**) Flow cytometric analysis of EpCAM expression in GFP and KuO double-positive cells derived from a primary ovarian tumor (i) and from a secondary ovarian tumor formed by transplantation of EpCAM^{POS} cells from the primary tumor (ii). EpCAM^{NEG} (iii) and EpCAM^{POS} (iv) cells derived from a primary ovarian tumor were maintained under adherent culture conditions for 2 weeks and then analyzed for EpCAM expression by flow cytometry. Shaded profiles were obtained with an isotype-matched control antibody. (**B**) Sphere-forming ability of sorted EpCAM^{POS} and EpCAM^{NEG} cells derived from primary tumors. Spheres were imaged by GFP and KuO fluorescence microscopy (scale bars, 500 μm), and the numbers of spheres formed from the indicated numbers of cells per well are presented as means ± SDs from three independent experiments. The number of spheres formed with a diameter of >100 μm was counted. $^{**}P < 0.01$. (**C**) Flow cytometric analysis of EpCAM, CD44 and CD117 expression in primary tumor-derived cells. Cells were stained with antibody to EpCAM as well as with antibodies to CD44 or to CD117.

Given that EpCAM^{POS} tumor cells showed metastatic ability, we next checked the expression of epithelial-mechenchymal transition regulatory genes, *Snail*, *Slug* and *Twist*. The expression level of *Snail* was slightly higher in EpCAM^{POS} cells than EpCAM^{NEG} cells, whereas the expressions of *Slug* and *Twist* were not associated with expression status of EpCAM (supplementary Figure 4 is available at *Carcinogenesis* Online). Thus, metastatic behavior of EpCAM^{POS} tumor cells was not simply due to the expression levels of these epithelial-mechenchymal transition regulatory genes.

p53 regulates expansion of ovarian stem-like tumor cells and tumor growth

In epithelial ovarian cancer, mutation or loss of p53 function is one of the most frequent genetic abnormalities (60–80%) (1) and high expression of EpCAM is correlated with poor prognosis (19). Furthermore, dysfunction of p53 pathway is frequently associated with undifferentiated histology in several types of epithelial ovarian cancer (23). Thus, we hypothesized that dysfunction of p53 pathway contributes to the expansion of EpCAM^{POS} stem-like cells and thereby

Table I. *In vivo* tumorigenicity of primary tumor-derived $EpCAM^{POS}$-, $EpCAM^{NEG}$- and hEpCAM-expressing $EpCAM^{NEG}$ cells

Primary tumor-derived cells	No. of transplanted cells						T-IC frequency (95% CI)
	10 000	5000	1000	500	100	10	
$EpCAM^{POS}$ cells	—	2/2	2/2	—	4/4	5/6	6.1** (2.6–15.7)
$EpCAM^{NEG}$ cells	2/2	3/3	6/7	3/10	0/12	0/10	988.6 (527.7–1852.4)
hEpCAM-expressing $EpCAM^{NEG}$ cells	—	—	5/5	5/5	4/5	2/5	45.2** (17.0–120.4)

Primary tumor-derived $EpCAM^{POS}$ and $EpCAM^{NEG}$ tumor cells were separated by FACS as in Figure 3A. The indicated numbers of $EpCAM^{POS}$-, $EpCAM^{NEG}$- or hEpCAM-expressing $EpCAM^{NEG}$ tumor cells were injected into the ovarian bursa of syngeneic mice. The incidence of tumor formation within 6 weeks was scored. Data represent the number of tumors per number of injections. T-IC frequencies were estimated with the use of ELDA software for limiting dilution analysis. $^{**}P < 0.01$.

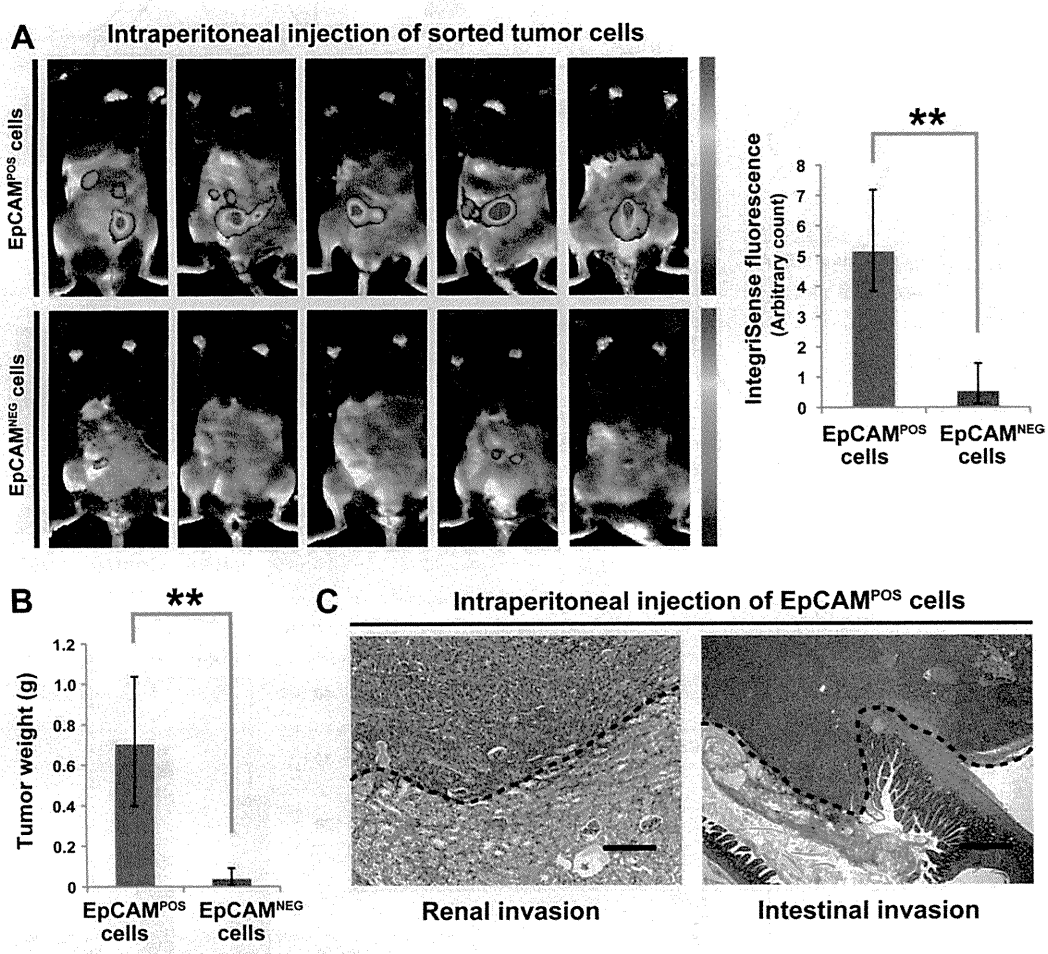

Fig. 4. Peritoneal metastasis by $EpCAM^{POS}$ tumor cells. (**A**) *In vivo* imaging of the IntegriSense signal in tumor-bearing mice. Representative volume renderings taken at the same color gating are shown for tumor-bearing mice at 14 days after intraperitoneal injection of primary tumor-derived $EpCAM^{POS}$ or $EpCAM^{NEG}$ cells (2×10^3). Total IntegriSense fluorescence (arbitrary counts) was also assessed at 14 days after cell injection, and the quantitative data are presented as means ± SDs for five mice. $^{**}P < 0.01$. (**B**) Total weight of disseminated tumors determined at 14 days after intraperitoneal injection of cells as in (**A**). Data are means ± SDs for five mice. $^{**}P < 0.01$. (**C**) Paraffin-embedded sections of disseminated tumors generated by $EpCAM^{POS}$ tumor cells were stained with H&E. Massive renal and intestinal invasion is apparent. Dotted lines indicate demarcation of the invasion front. Scale bars: 200 μm (left panel) or 500 μm (right panel).

impacts malignant behavior of epithelial ovarian cancer. To test this hypothesis, we next investigated whether p53 ablation might result in expansion of the $EpCAM^{POS}$ population among tumor cells and thereby promote tumor growth (Figure 5A). Quantitative RT–PCR analysis revealed that transfection of primary tumor-derived cells with p53 siRNA resulted in depletion of *p53* mRNA (Figure 5B). Flow cytometric analysis showed that the size of the $EpCAM^{POS}$ population among these tumor-derived cells was increased by transfection with p53 siRNA *in vitro* (Figure 5C), suggesting that p53 restricts the expansion of the $EpCAM^{POS}$ cell population. To examine the effect of this expansion of the $EpCAM^{POS}$ population on ovarian tumor development *in vivo*, we subcutaneously or orthotopically injected tumor cells transfected with control or p53 siRNAs into recipient mice. Tumor cells transfected with p53 siRNA showed enhanced tumor growth compared with those transfected with control siRNA (Figure 5D and E). Furthermore, Kaplan–Meier analysis revealed that the survival of recipients orthotopically injected with tumor cells transfected with p53 siRNA was reduced compared with that of those transplanted with tumor cells transfected with control siRNA (Figure 5F). These results suggested that the increase of numbers of $EpCAM^{POS}$ stem-like tumor cells by p53 ablation is

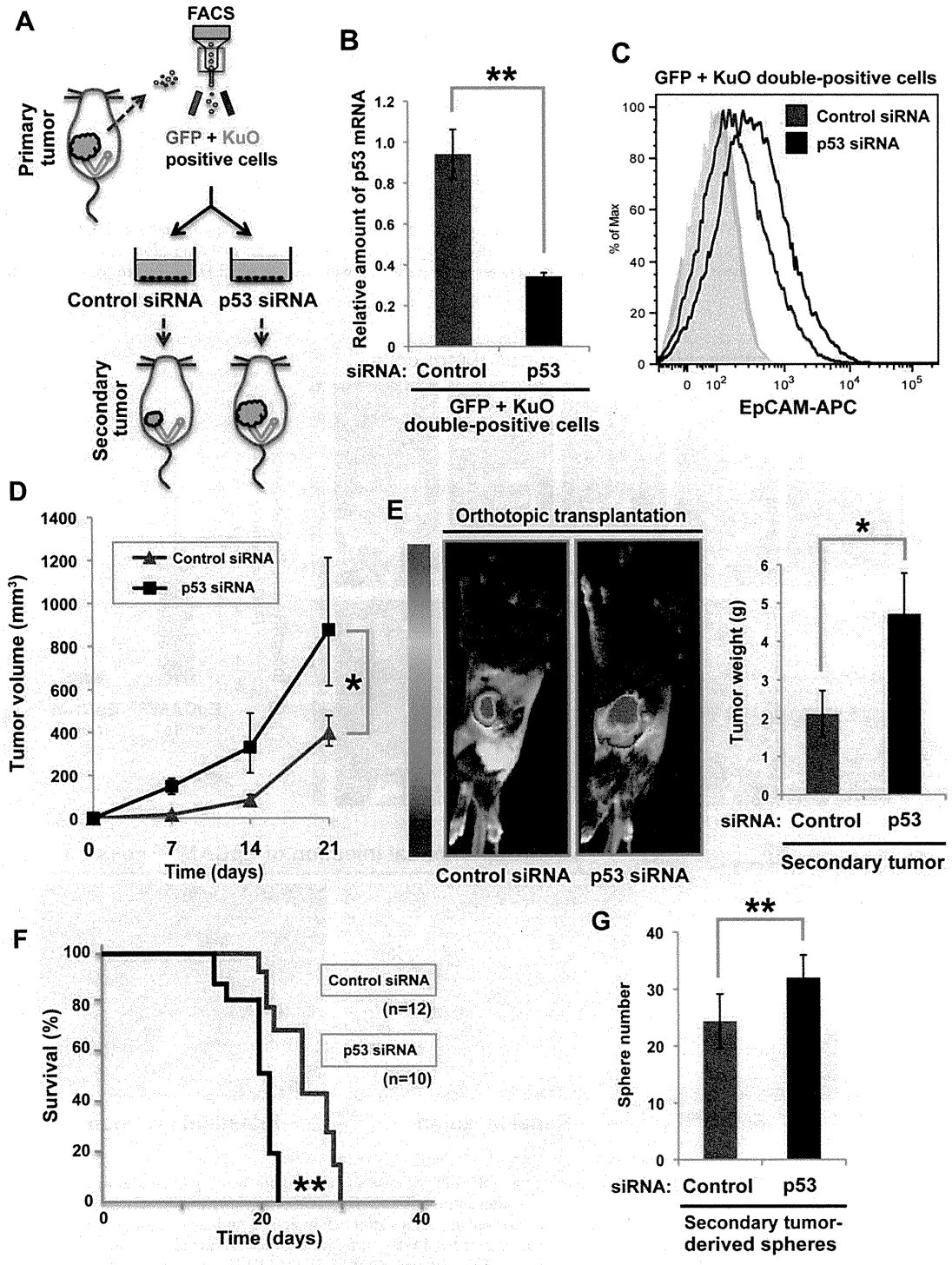

Fig. 5. p53 regulates the expansion of EpCAM^{POS} tumor cells and consequent ovarian tumor growth. (**A**) Experimental protocol. (**B**) Cells positive for both GFP and KuO were isolated from primary ovarian tumors, transfected with p53 or control siRNAs and subjected to real-time RT–PCR analysis of *p53* mRNA. Data were normalized by the amount of *GAPDH* mRNA and are means ± SDs from three independent experiments. $^{**}P < 0.01$. (**C**) Flow cytometric analysis of EpCAM expression in primary tumor-derived cells transfected with p53 or control siRNAs. (**D**) *In vivo* growth of primary tumor-derived cells transfected with p53 or control siRNAs. Cells (5×10^4) were implanted subcutaneously into the flank of immunocompetent mice. Data are means ± SDs for three mice. $^{*}P < 0.05$. (**E**) *In vivo* imaging of IntegriSense fluorescence in tumor-bearing mice. Primary tumor-derived cells (1×10^4) that had been transfected with p53 or control siRNAs were transplanted orthotopically into recipients at 14 days after transplantation. Quantitative data are means ± SDs for three mice. $^{*}P < 0.05$. (**F**) Survival curves for recipient mice transplanted orthotopically with primary tumor-derived cells (5×10^3) that had been transfected with p53 (blue, $n = 10$) or control siRNAs (gray, $n = 12$). $^{**}P < 0.01$. (**G**) Sphere-forming ability of GFP and KuO double-positive cells isolated from secondary tumors initiated by primary tumor cells transfected with p53 or control siRNAs. The cells were seeded in low-attachment plates at a density of 3×10^3 cells per well. Data are means ± SDs from three independent experiments. $^{**}P < 0.01$.

associated with tumor growth and poor prognosis in mouse ovarian cancer model.

To confirm that the enhancement of tumor growth by p53 knockdown was indeed due to the expansion of stem-like tumor cells, we investigated the frequency of stem-like tumor cells that possess sphere-forming ability. Cells isolated from the secondary tumors formed by the p53 siRNA-transfected cells yielded a significantly larger number of spheres compared with those isolated from the secondary tumors formed by control siRNA-transfected cells (Figure 5G). This result provided further evidence that the enhanced growth of tumors formed by p53 siRNA-transfected cells was associated with expansion of stem-like tumor cells. Together, these results suggested that the expansion of $EpCAM^{POS}$ stem-like tumor cells by p53 ablation enhances the malignant potential of epithelial ovarian cancer.

Discussion

We have identified a subpopulation of $EpCAM^{POS}$ cells as candidates for ovarian stem or progenitor cells that have the ability to yield CK8-expressing epithelial progeny. Furthermore, we established a mouse model of ovarian cancer by RNA interference-mediated transient knockdown of p53 followed by retroviral transduction of c-Myc and $K\text{-}Ras^{G12V}$ oncogenes in primary mouse ovarian $EpCAM^{POS}$ cells. Established mouse ovarian tumors manifested a hierarchical organization and contained stem-like tumor cells whose expansion was promoted by additional p53 ablation.

In normal mouse ovary, EpCAM-expressing cells were found to be localized predominantly in the proximity of the OSE and in the ovarian medulla near blood vessels. The expression of EpCAM in primary ovarian cells was downregulated after *in vitro* cultivation under normal conditions. Furthermore, $EpCAM^{POS}$ ovarian cells, but not $EpCAM^{NEG}$ cells, gave rise to CK8-expressing epithelial progeny *in vitro*. These findings are consistent with the results of previous studies showing that EpCAM expression is upregulated in somatic stem cells and is immediately downregulated during differentiation (29,33). $EpCAM^{POS}$ ovarian stem-like cells might therefore play a role in the maintenance and regenerative repair of the OSE as a result of their ability to yield CK8-expressing epithelial cells.

We also found that p53 knockdown induced the expansion of sphere-forming stem-like cells and promoted efficient retroviral transduction. Only $EpCAM^{POS}$ cells transfected with p53 siRNA formed tumors when transduced with the combination of c-Myc and $K\text{-}Ras^{G12V}$ oncogenes. $EpCAM^{POS}$ cells with normal p53 gene expression thus failed to form tumors even when transduced with both of these oncogenes. In addition, regardless of the level of p53 expression, $EpCAM^{POS}$ cells transduced with only a single oncogene (c-Myc or $K\text{-}Ras^{G12V}$) failed to form tumors. Together, these results indicated that transient suppression of the p53 pathway predisposes $EpCAM^{POS}$ ovarian cells to transformation by c-Myc and $K\text{-}Ras^{G12V}$. Furthermore, we found that EpCAM expression enhanced the tumor-forming ability in $EpCAM^{NEG}$ cells, indicating that EpCAM is a functional marker for mouse ovarian T-ICs. Consistent with our results, it has been recently reported that the expression of EpCAM confers the tumor-forming ability to non-tumorigenic human embryonic kidney 293T cells (9). Taken together, c-Myc and $K\text{-}Ras^{G12V}$ oncogenes enhance EpCAM expression and thereby promote the conversion of p53-silenced stem-like cells into T-ICs.

Poorly differentiated human breast tumors were recently shown to contain a higher number of CSCs than well-differentiated tumors, suggesting that CSC content affects biological and molecular heterogeneity of cancers (34). The tumor suppressor p53 was found to negatively regulate the self-renewal ability of CSCs as well as to reduce CSC content in an ErbB2 transgenic model of breast cancer (30). Furthermore, the absence of functional p53 has been shown to enhance the yield of induced pluripotent stem (iPS) cells, suggesting that p53 serves as a gatekeeper of self-renewal (35). In the present study, we found that RNA interference-mediated depletion of p53 triggers the expansion of $EpCAM^{POS}$ stem-like tumor cells that play a key role in ovarian tumor development. In human ovarian cancer, p53 mutation and EpCAM expression are frequently observed (36), and loss of p53 function has been associated with the pathogenesis of high-grade serous or undifferentiated adenocarcinoma of the ovary (37,38). Consistent with these clinical observations, ovarian carcinogenesis models based on oncogene-induced transformation of cells in which p53 is deficient or inactivated have been found to give rise to the development of undifferentiated tumors (39–43). Together, these findings suggest that dysfunction of the p53 pathway potentiates the self-renewal ability of ovarian stem-like tumor cells and thereby might affect the biological and molecular heterogeneity of ovarian cancers.

In conclusion, our experimental mouse model should facilitate further studies toward a comprehensive understanding of somatic stem cells and CSCs in ovarian tissue. Ultimately, such studies will be imperative to determine whether eradication of CSCs is critical for effective therapy.

Supplementary material

Supplementary Figures 1–4 can be found at http://carcin.oxfordjournals.org/

Funding

Ministry of Education, Culture, Sports, Science, and Technology of Japan (to O.N. and H.S.).

Acknowledgements

We thank I.Ishimatsu, S.Suzuki, Y.Ishii and S.Hayashi for technical assistance and K.Arai for help in preparation of the manuscript.

Conflict of Interest Statement: None declared.

References

1. Bast,R.C.Jr. *et al.* (2009) The biology of ovarian cancer: new opportunities for translation. *Nat. Rev. Cancer*, **9**, 415–428.
2. Reya,T. *et al.* (2001) Stem cells, cancer, and cancer stem cells. *Nature*, **414**, 105–111.
3. Visvader,J.E. *et al.* (2008) Cancer stem cells in solid tumours: accumulating evidence and unresolved questions. *Nat. Rev. Cancer*, **8**, 755–768.
4. Auersperg,N. *et al.* (2001) Ovarian surface epithelium: biology, endocrinology, and pathology. *Endocr. Rev.*, **22**, 255–288.
5. Okamura,H. *et al.* (2005) Pathophysiological dynamics of human ovarian surface epithelial cells in epithelial ovarian carcinogenesis. *Int. Rev. Cytol.*, **242**, 1–54.
6. Dubeau,L. (2008) The cell of origin of ovarian epithelial tumours. *Lancet Oncol.*, **9**, 1191–1197.
7. Kurman,R.J. *et al.* (2010) The origin and pathogenesis of epithelial ovarian cancer: a proposed unifying theory. *Am. J. Surg. Pathol.*, **34**, 433–443.
8. Herlyn,M. *et al.* (1979) Colorectal carcinoma-specific antigen: detection by means of monoclonal antibodies. *Proc. Natl Acad. Sci. USA*, **76**, 1438–1442.
9. Maetzel,D. *et al.* (2009) Nuclear signalling by tumour-associated antigen EpCAM. *Nat. Cell Biol.*, **11**, 162–171.
10. Spizzo,G. *et al.* (2004) High Ep-CAM expression is associated with poor prognosis in node-positive breast cancer. *Breast Cancer Res. Treat.*, **86**, 207–213.
11. Went,P. *et al.* (2006) Frequent high-level expression of the immunotherapeutic target Ep-CAM in colon, stomach, prostate and lung cancers. *Br. J. Cancer*, **94**, 128–135.
12. Stingl,J. *et al.* (2001) Characterization of bipotent mammary epithelial progenitor cells in normal adult human breast tissue. *Breast Cancer Res Treat*, **67**, 93–109.
13. Schmelzer,E. *et al.* (2006) The phenotypes of pluripotent human hepatic progenitors. *Stem Cells*, **24**, 1852–1858.
14. Tanaka,M. *et al.* (2009) Mouse hepatoblasts at distinct developmental stages are characterized by expression of EpCAM and DLK1: drastic change of EpCAM expression during liver development. *Mech. Dev.*, **126**, 665–676.

15. Dalerba,P. *et al.* (2007) Phenotypic characterization of human colorectal cancer stem cells. *Proc. Natl Acad. Sci. USA*, **104**, 10158–10163.
16. Al-Hajj,M. *et al.* (2003) Prospective identification of tumorigenic breast cancer cells. *Proc. Natl Acad. Sci. USA*, **100**, 3983–3988.
17. Yamashita,T. *et al.* (2009) EpCAM-positive hepatocellular carcinoma cells are tumor-initiating cells with stem/progenitor cell features, stem/progenitor cell features. *Gastroenterology*, **136**, 1012–1024.
18. Li,C. *et al.* (2007) Identification of pancreatic cancer stem cells. *Cancer Res.*, **67**, 1030–1037.
19. Spizzo,G. *et al.* (2006) Overexpression of epithelial cell adhesion molecule (Ep-CAM) is an independent prognostic marker for reduced survival of patients with epithelial ovarian cancer. *Gynecol. Oncol.*, **103**, 483–488.
20. Tashiro,H. *et al.* (1992) c-myc over-expression in human primary ovarian tumours: its relevance to tumour progression. *Int. J. Cancer*, **50**, 828–833.
21. Bell,D.A. (2005) Origins and molecular pathology of ovarian cancer. *Mod. Pathol.*, **18**, S19–S32.
22. Schuijer,M. *et al.* (2003) TP53 and ovarian cancer. *Hum. Mutat.*, **21**, 285–291.
23. Shih Ie,M. *et al.* (2004) Ovarian tumorigenesis: a proposed model based on morphological and molecular genetic analysis. *Am. J. Pathol.*, **164**, 1511–1518.
24. Shimizu,T. *et al.* (2010) c-MYC overexpression with loss of Ink4a/Arf transforms bone marrow stromal cells into osteosarcoma accompanied by loss of adipogenesis. *Oncogene*, **29**, 5687–5699.
25. Tamase,A. *et al.* (2009) Identification of tumor-initiating cells in a highly aggressive brain tumor using promoter activity of nucleostemin. *Proc. Natl Acad. Sci. USA*, **106**, 17163–17168.
26. Hu,Y. *et al.* (2009) ELDA: extreme limiting dilution analysis for comparing depleted and enriched populations in stem cell and other assays. *J. Immunol. Methods*, **347**, 70–78.
27. Nosaka,T. *et al.* (1999) STAT5 as a molecular regulator of proliferation, differentiation and apoptosis in hematopoietic cells. *EMBO J.*, **18**, 4754–4765.
28. Ishimoto,T. *et al.* (2011) CD44 variant regulates redox status in cancer cells by stabilizing the xCT subunit of system xc- and thereby promotes tumor growth. *Cancer Cell*, **19**, 387–400.
29. Lu,T.Y. *et al.* (2010) Epithelial cell adhesion molecule regulation is associated with the maintenance of the undifferentiated phenotype of human embryonic stem cells. *J. Biol. Chem.*, **285**, 8719–8732.
30. Cicalese,A. *et al.* (2009) The tumor suppressor p53 regulates polarity of self-renewing divisions in mammary stem cells. *Cell*, **138**, 1083–1095.
31. Barker,N. *et al.* (2009) Crypt stem cells as the cells-of-origin of intestinal cancer. *Nature*, **457**, 608–611.
32. Zhang,S. *et al.* (2008) Identification and characterization of ovarian cancer-initiating cells from primary human tumors. *Cancer Res.*, **68**, 4311–4320.
33. Schmelzer,E. *et al.* (2007) Human hepatic stem cells from fetal and postnatal donors. *J. Exp. Med.*, **204**, 1973–1987.
34. Pece,S. *et al.* (2010) Biological and molecular heterogeneity of breast cancers correlates with their cancer stem cell content. *Cell*, **140**, 62–73.
35. Hong,H. *et al.* (2009) Suppression of induced pluripotent stem cell generation by the p53-p21 pathway. *Nature*, **460**, 1132–1135.
36. Heinzelmann-Schwarz,V.A. *et al.* (2004) Overexpression of the cell adhesion molecules DDR1, Claudin 3, and Ep-CAM in metaplastic ovarian epithelium and ovarian cancer. *Clin. Cancer Res.*, **10**, 4427–4436.
37. Singer,G. *et al.* (2005) Patterns of p53 mutations separate ovarian serous borderline tumors and low- and high-grade carcinomas and provide support for a new model of ovarian carcinogenesis: a mutational analysis with immunohistochemical correlation. *Am. J. Surg. Pathol.*, **29**, 218–224.
38. Motohara,T. *et al.* (2010) Long-term oncological outcomes of ovarian serous carcinomas with psammoma bodies: a novel insight into the molecular pathogenesis of ovarian epithelial carcinoma. *Cancer Sci.*, **101**, 1550–1556.
39. Orsulic,S. *et al.* (2002) Induction of ovarian cancer by defined multiple genetic changes in a mouse model system. *Cancer Cell*, **1**, 53–62.
40. Flesken-Nikitin,A. *et al.* (2003) Induction of carcinogenesis by concurrent inactivation of p53 and Rb1 in the mouse ovarian surface epithelium. *Cancer Res.*, **63**, 3459–3463.
41. Dinulescu,D.M. *et al.* (2005) Role of K-ras and Pten in the development of mouse models of endometriosis and endometrioid ovarian cancer. *Nat. Med.*, **11**, 63–70.
42. Wu,R. *et al.* (2007) Mouse model of human ovarian endometrioid adenocarcinoma based on somatic defects in the Wnt/beta-catenin and PI3K/Pten signaling pathways. *Cancer Cell*, **11**, 321–333.
43. Sasaki,R. *et al.* (2009) Oncogenic transformation of human ovarian surface epithelial cells with defined cellular oncogenes. *Carcinogenesis*, **30**, 423–431.

Received March 29, 2011; revised July 15, 2011; accepted August 1, 2011

Clinical Features of Early-Stage Nonhydropic Mole for Diagnosis of Persistent Trophoblastic Disease

Junya Miyoshi, MD, Takashi Ohba, MD, PhD, Masaharu Fukunaga, MD, PhD, and Hidetaka Katabuchi, MD, PhD

OBJECTIVES: To characterize the clinical features of "nonhydropic" hydatidiform mole and to investigate regression of serum human chorionic gonadotropin (hCG) as an aid in detecting persistent trophoblastic disease after nonhydropic hydatidiform mole.

METHODS: Our study included women with histologically diagnosed nonhydropic molar pregnancies. Women did not exhibit macroscopic or characteristic ultrasonographic appearances specific to hydatidiform mole. Regression of serum hCG levels was compared with abortions of nonmolar pregnancies, which were histologically confirmed.

RESULTS: Among 34 nonhydropic molar pregnancies, 32 complete hydatidiform moles were analyzed, excluding two partial hydatidiform moles. Compared with nonmolar aborted pregnancies, pre-evacuation hCG levels were significantly higher in the 32 complete hydatidiform moles. The 32 molar pregnancies progressed to 24 cases of spontaneous remission and eight cases of persistent trophoblastic disease. Among patients with spontaneous remission, the time at which serum hCG levels became undetectable and the onset of first postabortion menstruation were similar to those in patients who had nonmolar abortions. In all patients who experienced regression, serum hCG was undetectable after the third postabortion menstruation. In all patients with persistent trophoblastic disease, serum hCG levels exceeded 25 milli-international units/mL 4 weeks after evacuation.

CONCLUSION: Without histological confirmation, it is difficult to diagnose nonhydropic molar pregnancy based solely on clinical presentation. Follow-up studies of serum hCG levels 4 weeks after abortion and after the third postabortion menstruation may aid in detecting impending persistent trophoblastic disease.

(Obstet Gynecol 2011;118:847–53)
DOI: 10.1097/AOG.0b013e31822adb8a

LEVEL OF EVIDENCE: II

From the Department of Obstetrics and Gynecology, Faculty of Life Sciences, Kumamoto University, Kumamoto, Japan; and the Department of Pathology, The Jikei University, School of Medicine, Tokyo, Japan.

Corresponding author: Junya Miyoshi, MD, Department of Obstetrics and Gynecology, Faculty of Life Sciences, Kumamoto University, 1-1-1 Honjo, Kumamoto 860-8556, Japan; e-mail: mjunshin@yahoo.co.jp.

Financial Disclosure
The authors did not report any potential conflicts of interest.

ISSN: 0029-7844/11

Over the past two decades, early detection of first-trimester pregnancy because of the widespread use of transvaginal ultrasonography and increased sensitivity in detecting reduced levels of human chorionic gonadotropin (hCG) have resulted in earlier diagnosis of hydatidiform mole. As a result, molar pregnancies do not necessarily present with classical symptoms such as enlarged uterus, preeclampsia, and hyperthyroidism.[1] The classical sonographic appearance of a complete mole has been described as a multivesicular intrauterine structure. The ultrasonographic appearance of a first-trimester molar pregnancy is nonspecific because the chorionic villi are not hydropic; therefore, the characteristic vesicular pattern is not present.[2] Clinicians may misdiagnose "nonhydropic" hydatidiform mole as spontaneous abortion of a nonmolar pregnancy if the aborted material is not histopathologically examined. Therefore, hCG derived from trophoblastic tissue is becoming a more important marker for gestational trophoblastic disease after nonhydropic hydatidiform mole. According to the International Federation of Gynecology and Obstetrics 2000 criteria,[3] persistent trophoblastic disease is diagnosed when a plateau or increase of consecutive hCG levels is observed after evacuation of the molar tissue. We report herein the clinical appearance of a nonhydropic hydatidiform mole and propose the regression of serum hCG levels

as an aid in detecting persistent trophoblastic disease after nonhydropic hydatidiform mole.

MATERIALS AND METHODS

From April 1999 through June 2009, 35 nonhydropic molar pregnancies were evacuated at Kumamoto University Hospital. These molar pregnancies demonstrated neither the characteristic multivesicular pattern on ultrasonographic examinations nor hydropic changes on macroscopic examination. The histopathological examination was performed by two pathologists (F.M. and H.K.) who independently examined hematoxylin and eosin–stained sections. The participants were enrolled in the study when the histopathological diagnosis of two pathologists agreed.

For the diagnosis of molar pregnancy, the pathologic criteria of Mazur and Kurman[4] can be used on specimens stained by hematoxylin and eosin. A complete mole is diagnosed when there is conspicuous trophoblastic proliferation, marked villous edema, and absence of an embryo. A partial mole is diagnosed when there is a mixture of edematous villi and normal-size villi, the presence of an embryo or fetus, and minimal focal trophoblastic proliferation.[5]

All patients were monitored by sequential serum hCG assays after evacuation of molar tissue. Follow-up of nonhydropic molar pregnancies after evacuation included a second evacuation performed 1 week after the first evacuation to ensure that no residual molar tissue remained in the uterine cavity.[6] Patients' serial serum hCG levels were followed-up until they decreased to less than 0.5 milli-international units/mL. Serum hCG should be undetectable by week 20; if the hCG level plateaus for 3 weeks, increase for 2 weeks, or exceeds the levels indicated to at any point during follow-up, then trophoblastic sequelae, ie, persistent trophoblastic disease, is diagnosed.

For the control, 24 healthy female volunteers who experienced spontaneous abortions that were histologically diagnosed as nonmolar pregnancies underwent serial serum hCG assays (January 2002–January 2007) after dilation and curettage.

Serial serum hCG levels were examined by enzyme immunoassay using antibodies against the carboxyl-terminal portion of the β-subunit until the concentration reached a level lower than the cut-off of 0.5 milli-international units/mL; hCG regression was analyzed along with the patient's clinical information. Results from nonhydropic molar pregnancies were then compared with the data from 24 abortions that were histologically diagnosed as nonmolar pregnancies.

The participants were recruited under the guidelines for protection of patient privacy in case reports, medical papers, and research meetings established by the Japanese Surgery Society Federation to protect personal information. This study was approved by the Kumamoto University's Institutional Review Board.

Statistical significance in parametrical data were evaluated by Student t test, and nonparametric data were assessed by Mann-Whitney U test. The values were deemed statistically significant at $P<.05$.

RESULTS

We initially determined the regression curve of plasma concentrations of hCG after a first-trimester nonmolar abortion until the concentration reached a level lower than the cut-off level of 0.5 milli-international units/mL. The median onset of first menstruation was 34 days, and that for complete disappearance of hCG was 60 days. This result is consistent with previous reports.[7,8]

Of the 35 nonhydropic molar pregnancies, the histological diagnosis was complete molar pregnancy in 32 cases, partial molar pregnancy in two cases, and inconclusive in one case. Three cases (two partial molar pregnancies and the inconclusive case) were excluded; thus, 32 patients with complete hydatidiform mole were analyzed. Rather than the classical ultrasonographic signs of hydatidiform mole, the so-called multivesicular pattern, nonhydropic hydatidiform moles appeared as thickened and echogenic intrauterine layers with an irregular surface without multicystic structures. Intrauterine anechoic fluid collection was commonly observed (Fig. 1A–C). In some cases, a cystic structure with irregular contours mimicking a gestational sac was seen in the uterine cavity (Fig. 1D–F), and a complex echogenic mass without multivesicular filling of the uterus was seen surrounded by several fluid-filled areas (Fig. 1G, H). However, these ultrasound findings were not always pathognomonic because similar findings were also observed in nonmolar aborted pregnancies (Fig. 1I).

In the 32 patients with nonhydropic hydatidiform mole, no significant differences were observed in maternal age (mean 30.8 compared with 32.4 years; $P=.42$), gestational age (mean 8.5 compared with 9.4 weeks; $P=.12$) at evacuation when compared with the 24 patients with nonmolar aborted pregnancies (Table 1). The pre-evacuation serum hCG levels in patients with early-stage molar pregnancies were higher than those of nonmolar aborted pregnancies (median 110,804 compared with 31,205 milli-international units/mL).

Of the 32 patients with molar pregnancies, 24 achieved spontaneous remission and eight had persistent trophoblastic disease develop. In the 24 patients

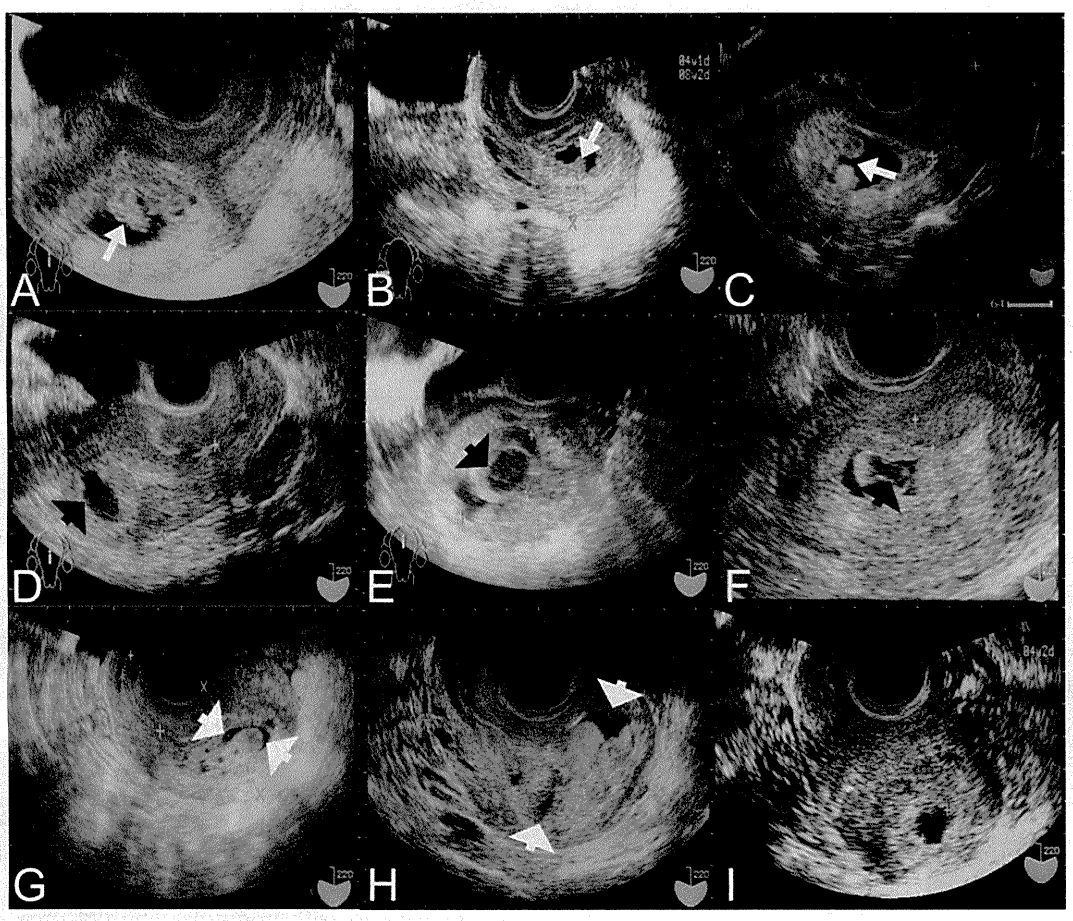

Fig. 1. Ultrasonographic findings of a nonhydropic hydatidiform mole. Early-stage hydatidiform mole appears as a thickened and echogenic intrauterine layer with an irregular surface (*white arrow*). Intrauterine anechoic fluid collection is commonly observed (**A, B, C**). In some cases, a cystic structure with irregular contours mimicking a gestational sac is seen in the uterine cavity (*black arrowhead*) (**D, E, F**). A complex echogenic mass without multivesicular filling of the uterus is surrounded by several fluid-filled areas (*white arrowheads*) (**G, H**). Cases in (**B**) and (**E**) progressed to persistent trophoblastic disease. A case of a nonmolar pregnancy demonstrating similar anechoic fluid collection with an irregular surface, mimicking early-stage hydatidiform mole, is shown as an example (**I**).

Miyoshi et al. Early-Stage Nonhydropic Molar Pregnancy. Obstet Gynecol 2011.

with molar pregnancies who achieved spontaneous remission, gestational age at evacuation was lower (mean 7.6 compared with 9.4 weeks; $P<.001$) and pre-evacuation hCG levels were higher (96,999 compared with 31,205 milli-international units/mL; $P<.01$) when compared with patients with nonmolar

Table 1. Comparison of Clinical Features of Patients With Nonmolar Aborted and Early-Stage Molar Pregnancy

	Early-Stage Molar Pregnancy (n=32)	Nonmolar Aborted Pregnancy (n=24)	*P*
Maternal age (y)	30.8 (27.6–33.9)	32.4 (30.3–34.5)	.42*
Gestational age on evacuation (wk)	8.5 (7.7–9.4)	9.4 (8.7–9.9)	.12*
Pre-evacuation hCG (milli-international units/mL) [median (range)]	110,804 (5,127–4,274,245)	31,205 (1,989–179,611)	<.001†

hCG, human chorionic gonadotropin.
Data are mean (95% confidence interval) unless otherwise specified.
* Student *t* test.
† Mann-Whitney *U* test.

Table 2. Clinical Course of Patients With Nonmolar Aborted and Nonhydropic Molar Pregnancy With Favorable Outcomes

	Early-Stage Molar Pregnancy; Spontaneous Remission (n=24)	Nonmolar Aborted Pregnancy (n=24)	*P*
Gestational age on evacuation (wk) [mean (95% CI)]	7.6 (7.1–8.1)	9.4 (9.7–9.9)	<.001*
Pre-evacuation hCG (milli-international units/mL)	96,999 (5,127–413,964)	31,205 (1,989–179,611)	<.01†
Postabortion hCG disappearance (d)	74 (32–126)	60 (20–118)	.08†
Onset of the first postabortion menstruation (d)	35 (23–104)	34 (25–84)	.60†

CI indicates confidence interval; hCG, human chorionic gonadotropin.
Data are median (range) unless otherwise specified.
* Student *t* test.
† Mann-Whitney *U* test.

aborted pregnancies (Table 2). The hCG regression curve was similar between nonmolar abortion and classical molar pregnancy with favorable outcomes, consistent with the previously report.[6] The time at which hCG became undetectable did not differ from that of patients with nonmolar pregnancies (median 74 compared with 60 days; *P*=.08) and did not correlate with pre-evacuation hCG levels. After evacuation, the first postabortion menstruation began at 35 days (23–104 days) in patients with molar pregnancies and at 34 days (25–84 days) in patients with nonmolar aborted pregnancies; these values were not statistically different.

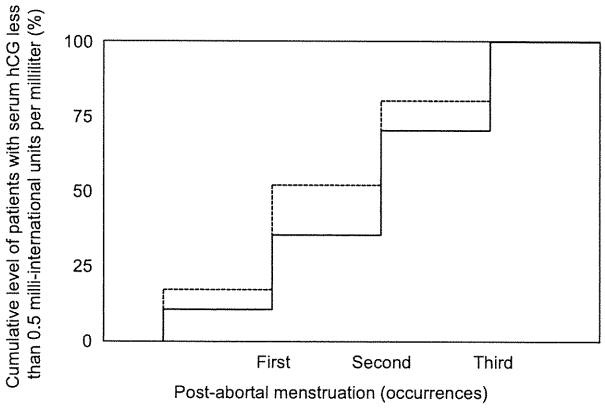

Fig. 2. Cumulative levels for patients with serum human chorionic gonadotropin (hCG) level less than 0.5 milli-international units per milliliter in molar pregnancies (spontaneous remission) compared with nonmolar aborted pregnancies by postabortion menstruation. The *solid line* depicts cumulative level for patients with serum hCG less than 0.5 milli-international Units per milliliter in molar pregnancies (spontaneous remission). The *dashed line* depicts the cumulative level of patients with serum hCG less than 0.5 milli-international units per milliliter in nonmolar aborted pregnancies. Cumulative level of patients with hCG less than 0.5 milli-international Units per milliliter increases after each postabortion menstruation. No patients were found to have a serum hCG more than 0.5 milli-international units per milliliter in spontaneous remission, nor did those patients with nonmolar aborted pregnancies before the fourth postabortion menstruation.

Miyoshi et al. Early-Stage Nonhydropic Molar Pregnancy. Obstet Gynecol 2011.

We next examined hCG regression in relation to postabortion menstruation (Fig. 2). The period from evacuation to the first postabortion menstruation did not correlate with pre-evacuation hCG levels. Eight (33%) of 24 patients with molar pregnancies achieved spontaneous regression before the second postabortion menstruation, and 17 (71%) achieved spontaneous regression before the third postabortion menstruation. Thirteen (54%) of the 24 patients with nonmolar aborted pregnancies achieved spontaneous regression by the second postabortion menstruation, and 19 (79%) achieved spontaneous regression by the third postabortion menstruation. The hCG levels were undetectable in all patients with spontaneous abortions and molar pregnancies after the third postabortion menstruation.

Clinical features were compared between persistent trophoblastic disease and spontaneous remission (Table 3). The mean maternal age was 35.0 years and the mean gestational age was 11.7 weeks at evacuation. There were no ultrasonographic findings before evacuation indicating the development of persistent trophoblastic disease (Fig. 1). However, the pre-evacuation hCG levels were higher than those for the 24 molar pregnancies with spontaneous remission (median 391,505 compared with 96,999 milli-international units/mL; *P*=.01). Serum hCG levels in the persistent trophoblastic disease patients began to increase at 24.6±10.9 days after evacuation (Fig. 3). However, mean serum hCG levels each week after evacuation were significantly higher than those in patients with molar pregnancies with spontaneous regression (the distribution overlapped). Seven of eight patients with persistent trophoblastic disease